UNIVERSITY OF OKLAHOMA

GRADUATE COLLEGE

IDENTIFYING THE CHEMICAL IMPACT AND THE MECHANISM OF AN ACCRETION OUTBURST ON A CLASS 0 PROTOSTAR

A THESIS

SUBMITTED TO THE GRADUATE FACULTY

in partial fulfillment of the requirements for the

Degree of

MASTER OF SCIENCE

By

RAJEEB SHARMA
Norman, Oklahoma
2019

IDENTIFYING THE CHEMICAL IMPACT AND THE MECHANISM OF AN ACCRETION OUTBURST ON A CLASS 0 PROTOSTAR

A THESIS APPROVED FOR THE
HOMER L. DODGE DEPARTMENT OF PHYSICS AND ASTRONOMY

BY

Dr. Nathan Kaib, Chair

Dr. John J Tobin

Dr. John Wisniewski

To my parents who believed in me and provided me with the resources to follow my passion. And to Deepika who encouraged me to continue.

Acknowledgements

Much of this thesis work would not have been possible without the help of my committee members and my research colleagues. I am particularly grateful to my advisor Dr. John J Tobin for the patience, support, and assistance he has provided throughout my Master's degree. He has been an excellent mentor, teaching me most of what I know about radio astronomy and protostar evolution. He has always guided me in the proper direction. A big thanks goes out to Dr. Patrick Sheehan for his invaluable knowledge on radiative transfer modeling, without which this thesis would not have been completed. I would also like to thank Nickalas Reynolds for his helpful hand over the years with Python codes for my research.

I wish to offer my special acknowledgment to my co-advisor Dr. Nathan Kaib for taking me under his wing and providing continued support and feedback throughout my research and preparation of this thesis. Also, I would like to thank Dr. John Wisniewski for being my committee member and providing a new perspective on my research.

This research used in this thesis was supported by NSF Astronomy and Astrophysics Grant #AST-1814762. The Submillimeter Array is a joint project between the Smithsonian Astrophysical Observatory and the Academia Sinica Institute of Astronomy and Astrophysics and is funded by the Smithsonian Institution and the Academia Sinica. I would like to recognize and acknowledge the very significant cultural role and reverence that the summit of Mauna Kea

has always had within the indigenous Hawaiian community. I am most fortunate to have the opportunity to conduct observations from this mountain. This paper makes use of the following ALMA data: ADS/JAO.ALMA#2015.1.00041.S. ALMA is a partnership of ESO (representing its member states), NSF (USA) and NINS (Japan), together with NRC (Canada), MOST and ASIAA (Taiwan), and KASI (Republic of Korea), in cooperation with the Republic of Chile. The Joint ALMA Observatory is operated by ESO, AUI/NRAO and NAOJ. The National Radio Astronomy Observatory is a facility of the National Science Foundation operated under cooperative agreement by Associated Universities, Inc.

Table of Contents

List of Figures

List of Tables

Abstract

Past and present observations of luminosity bursts in various young protostars provide increasing evidence that episodic accretion is a common phenomenon in protostellar evolution. Studying these outbursting systems can help reveal the dynamics of mass accretion in protostars and constrain the properties and nature of protostellar disks. I present a study of the youngest known outbursting protostar, HOPS 383, a Class 0 protostar in the Orion molecular cloud using observations from the Submillimeter Array (SMA), the Atacama Large Millimeter/submillimeter Array (ALMA), and the Very Large Array (VLA). First, I use the SMA to study the effect of the outburst on the chemistry of the disk and the envelope around HOPS 383. The SMA observations show peaked HCO^+ and $H^{13}CO^+$ and reduced N_2H^+ at the protostar position, consistent with chemical models of outbursting YSOs where the evaporating CO increases HCO^+ and decreases N_2H^+. Second, I present dust continuum observed with the ALMA at 0.87 mm and the VLA at 9 mm to constrain the disk properties and understand its role in protostellar evolution. Both the continuum show a well-resolved disk orthogonal to the outflow. The outflow is traced by ^{12}CO, evident both in the SMA and the ALMA data, suggesting that HOPS 383 is quite young. Assuming isothermal and optically thin dust emission, I estimate the current disk mass between 0.043 $M_\odot$ and 0.15 $M_\odot$. To assess of gravitational instability (GI) as the cause of the outburst, I calculate Toomre's Q ~1.14 and ~0.87 pre-outburst, using the ALMA and the VLA derived disk masses, respectively. Finally, modeling the resolved continuum from the ALMA and the VLA using 3D radiative transfer code gives disk masses of 0.1 $M_\odot$ and 0.065 $M_\odot$ for the ALMA only models and disk masses of 0.25 $M_\odot$ and 0.21 $M_\odot$ for the ALMA+VLA models. The disk temperature and surface density profiles from the modeling suggest that Toomre's $Q < 1$ for most cases before the outburst, suggesting that GI possibly drove the outburst in HOPS 383 and is a viable mechanism to explain outbursts at an early age if the disk is sufficiently massive.

Chapter 1

Introduction

Giant molecular clouds (GMCs) found in the interstellar medium are the prominent sites of star formation. These GMCs are predominantly composed of H_2 gas and dust, and have regions that are opaque to optical and ultraviolet light with the dust blocking most of the interstellar radiation. Hence, they have very cold interiors with average temperatures of $\sim$10 - 20 K. GMCs are thought to be gravitationally bound and have highly supersonic and turbulent velocity fields (Evans 1999, Zuckerman & Evans 1974). The turbulent flows can collide and shock, collecting mass in certain regions and inhibiting mass accumulation in others, creating regions of higher density of gas and dust called clumps in the clouds (Goldsmith 1987; Shu et al. 1987; Lada & Lada 2003; Mac Low & Klessen 2004). These high-density clumps of low temperature are the ideal sites for star formation.

The timescales of turbulence to decay in the GMC are much shorter than the cloud lifetime of $\sim$10 Myr. Hence, along with the internal pressure, the turbulence helps to initially stabilize the cloud on a global scale from collapsing under its own gravity. Due to its turbulent nature, clumps in the cloud may locally have angular momentum on smaller scales even though the cloud, on the whole, may have a zero net angular momentum. Under the right circumstances, these high-density clumps can become gravitationally unstable and their inner regions collapse, accreting material from the surrounding clump and cloud. As a clump collapses to a protostellar core, its dimensions shrink by many orders of magnitude, requiring the core to spin more rapidly to conserve angular momentum. This makes it easier for material to fall in near the protostar from the poles than the equator. Thus, the material that revolves around the equator falls in more slowly and gets "held back" by rotation and eventually flattens to form a disk around the protostar (Shu et al. 1987; McKee & Ostriker 2007). The protostellar collapse phase is fairly rapid and has a timescale of $\sim 10^5$ yr (Dunham et al. 2014). The disk also rapidly evolves during this time, changing its size and mass. Protostellar disks are composed of dense rotating gas and dust, fed by an accreting envelope surrounding the protostar. Initially, the disk consists of material with a similar composition as the molecular cloud (Visser et al. 2011); this dusty and gaseous material evolves forming larger grains which settle to the mid-plane of the disk.

1.1 Protostellar Evolution

Protostellar systems are observed at a variety of evolutionary states and their observed characteristics are different. The spectral energy distribution (SED) is a key indicator to reveal the evolution of a protostar. Protostellar systems are classified into groups ranging from Class I to Class III, based on their SEDs in the infrared between 2 - 25 μm (Lada & Wilking 1984; Lada et al. 1987). The classification scheme defines the spectral index as

$$\alpha = \frac{d\,\log(\lambda \mathrm{F}_{\lambda})}{d\,\log(\lambda)}, \tag{1.1}$$

where λ is the wavelength, and F_λ is the flux density at λ with the classes defined as,

- Class I: $0 < \alpha \leq 3$, source SED contains large infrared excess above a stellar photosphere.
- Class II: $-2 < \alpha \leq 0$, source SED contains infrared excess above a stellar photosphere, but smaller than Class I phase.
- Class III: 0 $-3 < \alpha \leq -2$, source SED contains mostly stellar photosphere, very little excess infrared emission, if at all.

Additionally, André et al. (1993) added a new class, Class 0, to account for the most embedded protostars, completely veiled in the near to mid-infrared, at least to the instruments at that time. The Class 0 protostars have a high ratio of submillimeter luminosity (L_{submm}) to bolometric luminosity (L_{bol}). Example of SEDs of all the classes of protostellar systems is shown in Figure 1.1. However, we note that Class 0 can have emission detected shortward of 10 μm, while the diagram suggests otherwise (Tobin et al. 2007). In addition to the spectral index and L_{submm}/L_{bol}, another quantity often used to classify young stellar objects (YSOs) is the bolometric temperature (T_{bol}): the effective temperature of a blackbody having the same mean frequency as the observed continuum spectrum (Myers & Ladd 1993; Chen et al. 1995). According to the T_{bol} classification scheme, Class 0 YSOs have $T_{bol} \lesssim 70$ K, Class I YSOs have $70 \text{ K} \lesssim T_{bol} \lesssim 650$ K, Class II YSOs have $650 \text{ K} \lesssim T_{bol} \lesssim 2800$ K, and Class III YSOs have $T_{bol} > 2800$ K.

Physically, the protostar class relates to the evolutionary state of a YSO. Class 0 YSOs are the youngest objects with the system characterized by a dense infalling envelope (André et al. 1993). Class I sources are less embedded than Class 0 sources but are still dominated by their envelope. Class II YSOs are pre-main sequence stars that have shed their envelopes and only a dusty protostellar disk remains. Finally, Class III sources have most of their disk material accreted or converted into large bodies (e.g. planetesimals). This thesis primarily focuses on the youngest Class 0 disks and their significance and impact of accretion bursts on the evolution of such young systems.

Protoplanetary disks are well-established and studied around pre-main-sequence stars. A disk can be considered protoplanetary and not protostellar once the envelope has been accreted or dissipated, nearly concluding the star formation process. Class III YSOs have most of the dust processed and the disk is mostly made of larger dust grains and planetesimals (Williams & Cieza. 2011). By the beginning of the Class II phase, which starts about ∼0.5 Myr after the formation of a star (Evans et al. 2009; Dunham et al. 2014), the envelope feeding the disk is largely dissipated. Hence, most of the stellar mass accretion by the protostar is expected to occur during the Class 0 and Class I stage. These protostellar disks not only accrete mass onto the stars, building up the mass of the protostar, but the disks are the initial conditions for the later proto-planetary disks (Testi et al. 2014). To understand the formation and evolution of these protostellar systems and their disks, it is necessary to observe disks in their infancy, which helps us understand the early stages of star formation. A few Class 0 systems with rotationally supported disks have been observed (Tobin et al. 2012; Murillo et al. 2013; Codella et al. 2014; Lindberg et al. 2014; Aso et al. 2015; Yen et al. 2017; Tobin et al. 2018). Even though the sample size is small, studying these systems can help shed some light into the physical and chemical processes of early star formation.

A fundamental problem of star formation is how stars accrete their mass. Due to the highly embedded nature of Class 0 and I protostars, mass accretion is much more difficult to observe directly as compared to later phases. However, the total radiative output during the Class 0 and I phase is likely dominated by accretion luminosity (Evans et al. 2009; Dunham et al. 2010). Hence, we can infer an indirect measurement of the accretion rate of a protostar by calculating its luminosity. The luminosity can be found from the SED of the protostar, giving us clues about the formation timescale and the accretion process. However, the significant number of low-luminosity protostars observed creates a picture which is largely inconsistent with predictions of idealized star formation theory.

1.2 The Luminosity Problem

An idealized model of star formation consists of an inside-out collapse of an isothermal sphere (Shu 1977). The collapse proceeds inside-out, with a rarefaction wave propagating outward, inside of which material falls in free-fall at a constant mass accretion rate of $\sim$2 - 5 $\times$ 10^{-6} $M_\odot$ yr^{-1} (Shu 1977; Terebey et al. 1984). Such steady-accretion models predict protostellar luminosities of order 10 - 20

$L_\odot$ to build a star of average mass (0.5 $M_\odot$). However, the median luminosity of protostars is observed to be of order 1 - 3 $L_\odot$ (Kenyon et al. 1990). This discrepancy between the observed luminosities and the predicted luminosities of the inside-out collapse model is known as the "luminosity problem". Other studies that include magnetic fields (Galli & Shu 1993; Li & Shu 1997; Basu 1997), non-zero initial inward motion (Larson 1969; Penston 1969; Hunter 1977; Fatuzzo et al. 2004), collapse of isothermal spheres of constant density (Foster & Chevalier 1993; Henriksen et al. 1997) typically have higher accretion rates, which only exacerbates the problem.

When the luminosity problem was first identified, Taurus was the only major molecular cloud that was well-studied. However, it was further emphasized by observations from other regions. Results from the *Spitzer Space Telescope* "From Molecular Cores to Planet Forming Disks" (*Spitzer* c2d) program gave further observational evidence for the luminosity problem. The c2d program observed five nearby star-forming molecular clouds and discovered Very Low Luminosity Objects (VeLLOs) embedded in dense cores (Evans et al. 2003; Evans et al. 2009). Analyzing the population of protostars as a whole, Evans et al. (2009) and Dunham et al. (2010) found an extinction-corrected median luminosity of 1.5 $L_\odot$, strongly indicating that the distribution is skewed towards low luminosities. Even after including the 350 μm data for the much brighter sources, they were only able to get the median to 5.3 $L_\odot$, justifying the validity of the luminosity problem. Fischer et al. (2017) conducted an extensive survey of the protostars in Orion as part of the *Herschel* Orion Protostar Survey (HOPS) and found that the luminosity problem persists in Orion as well.

1.3 Solving the Luminosity Problem

Kenyon et al. (1990) suggested several mechanisms to resolve the luminosity problem. Two of the major solutions include slow accretion and episodic accretion. I mostly focus on the episodic accretion scenario but also briefly explain the slow accretion scenario here.

The slow accretion scenario increases the length of the protostellar accretion phase, by decreasing the accretion rate. Previously, the protostellar lifetime was thought to be ∼0.1 Myr (Lada et al. 1987; Kenyon et al. 1990). However, following the *Spitzer* c2d observations of several GMCs, Evans et al. (2009) inferred mean lifetime of ∼0.5 Myr. This longer lifetime helps to alleviate the problem by lowering the accretion rate to $\simeq 10^{-6}$ $M_\odot$ yr^{-1}, which corresponds to a luminosity of about 2.2 $L_\odot$. However, even though the slow accretion scenario almost resolves the median luminosity, it does not account for the spread of luminosities over several order of magnitudes for the protostars. This suggests that slow accretion is not the complete picture.

1.3.1 Episodic Accretion

The second scenario proposed by Kenyon et al. (1990) suggests that the accretion is not constant but highly variable, such that much of the protostellar mass would be accreted in several bursts of high accretion. In this case, protostars spend most of their time in low-luminosity, low-accretion phase, but series of brief, intense accretion bursts over the star formation period accrete the majority of the protostellar mass (Hartmann & Kenyon 1996). Such episodic accretion would explain the spread of luminosities of the protostars. The first system detected, now recognized as an accretion driven outburst, was FU Orionis in 1936 (Wachmann 1939), a pre-main sequence star. Since then, however, improved infrared surveys have found several younger Class I protostars undergoing outbursts (e.g., Graham & Frogel 1985; Ábrahám et al. 2004; Fischer et al. 2012). These outbursts are thought to reflect a sudden increase in accretion rate to $\gtrsim 10^{-4}$ $M_\odot$ yr^1, enabling the protostar to acquire most of its mass during these bursts (Vorobyov & Basu, 2005, 2006). Based on the number of known outbursting protostars, Offner & McKee (2011) estimated that roughly 25% of the total mass accreted by protostars within 1 kpc can be accounted to the outbursting protostars.

Based on the 5 known outbursts in 60 years of observation and star formation rate of 0.01 stars yr^{-1}, Hartmann & Kenyon (1996) remarked that a protostar should undergo about 10 bursts in its lifetime. So, if most of the mass is accreted during these bursts, then these bursts should be seen throughout the protostellar phase (Vorobyov & Basu 2006). Although accretion bursts were observed in several Class I and II objects, the youngest protostars, the Class 0 objects, did not have detected outbursts. However, Safron et al. (2015) were able to identify an outburst in HOPS 383, a Class 0 protostar, around the year 2006, making it the youngest known outbursting YSO.

The mechanism driving such accretion bursts has been widely debated. One of the favored scenarios is that accretion outbursts are initiated by gravitational instability (GI) in the protostellar disk (Vorobyov & Basu 2005). As the disk continues to gain mass from the surrounding envelope, GI can lead to formation of clumps in the disk, which are driven into the protostar by gravitational torques, generating high luminosity outbursts. In addition to GI, magnetorotational instability (MRI) might also explain outbursts in protostars (Armitage et al. 2001). MRI mostly operates on the inner disk where the protostar can thermally ionize the material. Zhu et al. (2007) and Zhu & Hartmann (2009) showed that both GI and MRI are needed to explain the protostellar infall rates over the large range of radii needed to explain the FU Ori outburst. The accretion bursts stop when most of the material from the infalling envelope is accreted. In this thesis, I will attempt to test GI as a cause of outburst in HOPS 383. Using continuum observations and radiative transfer modeling, I will examine the stability of the disk around the protostar and discuss GI as a potential explanation of the outburst.

Such accretion bursts leave their trace, changing the chemistry and radial abundance of molecular species around the protostar. Observing the molecular tracers around protostars can help us observe the effects of luminosity bursts. The increase in temperature due to the burst releases the CO molecules that were frozen-out on the dust grains which react with molecules in the envelope. Specifically, the released CO reacts with N_2H^+ in the envelope, forming HCO^+ as a byproduct (Visser & Bergin 2012; Visser et al. 2015). The variation in luminosities due to an accretion burst also extend the central $C^{18}O$ emission by shifting the radius of sublimation outward from its steady-state (Jørgensen et al. 2015). In this thesis, I will present the results of observations of these tracers around HOPS 383 after the outburst. This will help us constrain the chemical signatures of outbursts, providing new means to identify protostars that have recently undergone outburst.

1.4 Thesis Overview

This thesis investigates the protostellar system of HOPS 383 to understand the mechanism and the chemical effects of the outburst on its environment. I use various radio telescope observations to trace the molecular signatures and continuum emission of the protostar. Chapters 2, 3, and 4 are largely based on the paper by Sharma et al., 2019 in preparation. In Chapter 2, I use the Submillimeter Array (SMA) observations of HOPS 383 to study the chemical effects of the outburst on the protostar. I will present the various molecular lines found by the SMA in multiple bands and will look for the predicted chemical signature of the outburst by focusing on N_2H^+ and $H^{13}CO^+$. Chapter 3 focuses on the Atacama Large Millimeter/submillimeter Array (ALMA) and the Very Large Array (VLA) observations of the continuum emission of HOPS 383. The continuum data is used to extend the SED of HOPS 383 to millimeter and centimeter wavelengths. I also use the continuum emission to calculate the mass of the disk around HOPS 383 to study its stability. Chapter 4 details the radiative transfer modeling of HOPS 383 using the continuum visibilities from the ALMA and the VLA and the SED from literature. Finally, Chapter 5 summarizes the conclusion from the thesis and presents the next steps to consider following this study.

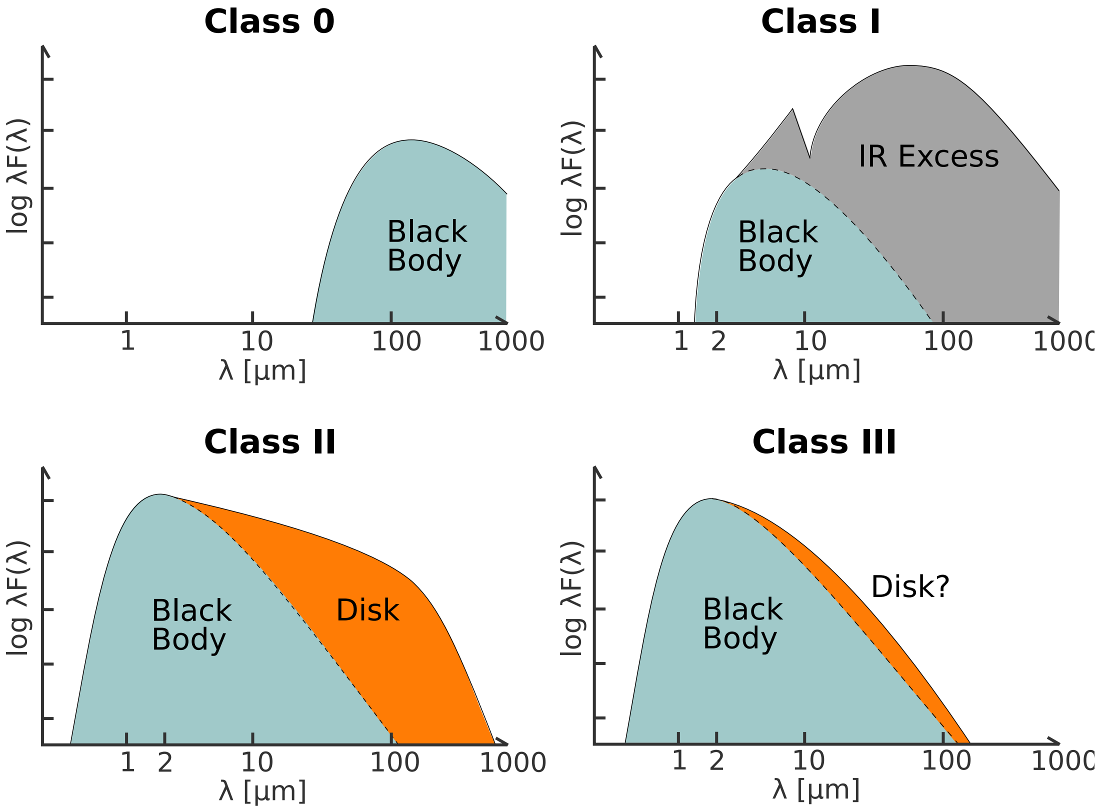

Fig. 1.1.—: Figure outlining the general shape of the SED of different stages of protostellar evolution. Class 0 protostars are mostly visible at $\lambda \gtrsim 25\mu$m and their emission is predominantly due to isothermal dust. Class I protostars have excess infrared radiation from the dust envelope overshadowing that of blackbody radiation. Class II protostars have shed their envelopes, and only the dusty disk remains, shown by the infrared excess in the SED. The width of the spectrum is much wider than that of a blacobody. Class III protostars have shed most of their disk and only few large debris remain. The SED is comparable to that of a blackbody radiation. This figure is reproduced from Persson (2014).

Chapter 2

Constraining the Chemical Signatures of Episodic Accretion on HOPS 383: Interferometric Molecular Line Mapping

2.1 Introduction

Episodic accretion bursts have the ability to significantly alter the chemical composition of the protostellar envelope and the disk (e.g., Visser & Bergin 2012; Visser et al. 2015; Jørgensen et al. 2015). These chemical effects primarily result from the change in temperature of the surrounding gas and dust due to the luminosity increase by $\sim$100×. The increase in temperature can evaporate the CO molecules that were frozen on the icy grain mantles, releasing them back into the gas phase (Lee et al. 2007; Visser & Bergin 2012; Visser et al. 2015; Vorobyov et al. 2013). Since the freeze-out timescale of CO at protostellar envelope densities is longer than the duration of the bursts, the effects of the burst can be seen long after the actual burst has occurred (Jørgensen et al. 2015; Visser et al. 2015). The increase in luminosity can also alter the D/H ratio of water and other chemical species, triggering a series of changes in the molecular composition of the envelope (Owen & Jacquet 2015).

HOPS 383 is located in the Orion Molecular Cloud 3 (OMC3) region and was classified as a protostar in the *Spitzer* (Megeath et al. 2012) and *Herschel Orion Protostar Survey* (Furlan et al. 2016; Fischer et al. 2017). It went through an outburst around the year 2006 which is most prominently seen at a wavelength of

24 μm. The luminosity at this wavelength increased from ∼0.2 $L_\odot$ to ∼7.5 $L_\odot$ in between 2004 and 2008. Figure 2.1 shows the near- and mid-infrared images of HOPS 383 before and after the outburst. Furthermore, IR to sub-mm follow-up of HOPS 383 shows no notable signs of decline in luminosity (Safron et al. 2015). Given the length of the outburst and the lack of decrease in luminosity, it mimics the characteristics of FU Orionis type outbursts, indicating that such outbursts are possible in the protostellar phase as well.

The accretion burst in HOPS 383 provides a rare opportunity to observe the physical and chemical effects of an accretion burst on a protostellar envelope. Since the infalling envelopes are very dense in this phase, the continuum and molecular line emission of Class 0 objects are entangled with that of the disk (Tobin et al. 2018). Thus the properties of Class 0 disks such as their mass, radii, and temperature have not been classified for a broad sample. So it is unclear if processes such as gravitational instability play an important factor at such a young stellar age. Constraining the cause, effects, and timescales of accretion bursts will enable us with new means to identify protostars that have undergone bursts in the past and may in the future.

In this chapter, we report the molecular line results of ^{12}CO, ^{13}CO, C^{18}O, N_2H^+, HCO^+, and $H^{13}CO^+$ from the Submillimeter Array (SMA) in multiple configurations. The observations and data reduction are described in Section 2.2. The empirical results from the observations are presented in Section 2.3. The implications of our results are discussed in Section 2.4 and the conclusions are presented in Section 2.5.

2.2 SMA Observation and Data Reduction

We used the SMA located on Mauna Kea, Hawaii in the Extended and the Subcompact configuration to observe HOPS 383 between October 2015 and November 2016. The Subcompact configuration was sensitive to the integrated emission of molecules but only gave a resolution of $4''$-$7''$ ($\sim$1700 - 3000 AU). Combining Extended configuration data gave us a resolution of $\sim 1''$ (420 AU) which allows us to resolve the expected emission of various molecular lines.

2.2.1 Subcompact Observations

The Subcompact observations were conducted on 27 October 2015 using 6 antennas and on 04 November 2015 using 8 antennas for a total time on source of 4.7 hr, 3.6 hr, and 7.5 hr for wavelengths of 850 mum, 1.1 mm and 1.3 mm, respectively. The flux, bandpass, and complex gain calibrations were carried out using Uranus, 3C279, and 0607-085, respectively. We used three different tunings centered at $\sim$225.5 GHz, $\sim$267.5 GHz, and at $\sim$351 GHz in the Subcompact configuration. The 225.5 GHz and 351 GHz observations were conducted in dual-receiver, 2 GHz mode. This setup covered ^{12}CO, ^{13}CO, C^{18}O ($J = 2 \rightarrow 1$), HCO$^+$ ($J = 4 \rightarrow 3$), and H^{13}CO$^+$($J = 4 \rightarrow 3$). The 267.5 GHz tuning used a single-receiver, 2 GHz mode to observe the continuum and N$_2$H$^+$ ($J = 3 \rightarrow 2$), HCO$^+$ ($J = 3 \rightarrow 2$), and H^{13}CO$^+$ ($J = 3 \rightarrow 2$) lines. Our setup was also intended to observe the H$_2$CO ($J = 3_{0,3} \rightarrow 2_{0,3}$), SiO ($J = 5 \rightarrow 4$), and SO ($J_N = 5_6 \rightarrow 4_5$) lines but we could not observe these lines due to problems with the correlator.

2.2.2 Extended Observations

The Extended observations were conducted on 20 November 2016 and on 27 November 2016 using 8 antennas for a total time on source of 5.9 hr and 2.8 hr for wavelengths of 1.1 mm and 1.3 mm, respectively. For the 20 November observation, Uranus was used as the flux calibrator and for the 27 November observation, both Uranus and Callisto were used as the flux calibrators. Bandpass and complex gain calibrations for both observations were carried out using 3C279 and 0607-085, respectively. Just like the Subcompact, we used three tunings centered at ∼225.5 GHz, at ∼267.5 GHz, and at ∼351 GHz in the Extended configuration. We observed the same spectral setup as in the Subcompact configuration, but were able to also observe the H_2CO ($J = 3_{2,1} \rightarrow 2_{2,1}$), SiO ($J = 5 \rightarrow 4$), and SO ($J_N = 5_6 \rightarrow 4_5$) lines.

2.2.3 Data Reduction

Calibration and editing of the SMA data were performed using the IDL based MIR software package. MIR was originally developed for the Owens Valley Radio Observatory and adapted by the SMA group. The imaging of both the continuum and the spectral line data were performed using the MIRIAD (Multichannel Image Reconstruction, Image Analysis and Display; Sault et al. 1995) software package.

2.3 Results

2.3.1 Molecular Line Results

The spectral setup of the SMA covers N_2H^+, N_2D^+, HCO^+, and $H^{13}CO^+$ molecular lines, which were the key lines of interest. We show the integrated intensity (moment zero) maps from the combined Subcompact and Extended configuration, overlaid on the 1.3 mm SMA continuum for these molecular lines in Figure 2.2 and Figure 2.3. The peak signal-to-noise ratio of these transitions is ∼5-7 σ in 0.25 kms^{-1} channels. These molecules serve as complementary tracers that allow us to test the predictions of chemical models by Visser et al. (2015).

N_2H^+ and N_2D^+ trace the cold dense regions (n $\sim 10^5$ cm^{-3}, $T \lesssim 20$ K) around the protostar and its envelope where CO is mostly frozen out (e.g. Bergin & Tafalla 2007; Visser & Bergin 2012). We see N_2H^+ appearing marginally double-peaked about ∼250 AU around the protostar position in Figure 2.2. HCO^+ will form as a by-product of gas-phase CO reacting with N_2H^+. So, HCO^+ should be present with a higher concentration at inside R ∼500 AU where the increase in luminosity converts the frozen out CO to gas-phase, converting N_2H^+ to HCO^+. In Figure 2.3, we see that HCO^+ is peaked at the protostar position, corresponding to the warmer regions where we observe the decrease in N_2H^+. We also detect N_2D^+ and $H^{13}CO^+$ as shown in Figures 2.2 and 2.3 around HOPS 383 with similar spatial distributions to N_2H^+ and HCO^+, respectively. Although the surface brightness of N_2D^+ does not peak as strongly as that of N_2H^+, somewhat resembling the structure of N_2H^+ and N_2D^+ toward L1157-mm (Tobin et al. 2013).

The spectral setup also detected the $C^{18}O$ ($J = 2 \rightarrow 1$) and H_2CO ($J = 3_{0,3} \rightarrow 2_{0,3}$) emission above the 3σ level. Figure 2.4 shows the integrated intensity map of the blue- and red-shifted emission from the combined Extended and Subcompact configuration for the $C^{18}O$ and the Subcompact configuration for the H_2CO overlaid on the 1.3 mm SMA continuum. However, the $C^{18}O$ data cube is contaminated by a foreground cloud that is also emitting at a similar velocity range, which mostly affected the blue-shifted emission. Therefore, the $C^{18}O$ emission must be used with caution. H_2CO is peaked near the protostar because it is warmer, suggesting that H_2CO was frozen-out in the dust grains before the outburst. Comparing with Figure 2.5, unlike ^{12}CO, $C^{18}O$ is not significantly affected by the outflow from HOPS 383. This is mainly because $C^{18}O$ is mostly optically thin and highly sensitive to the inner 1000 AU radii near where CO is evaporated from the dust grains (Jørgensen et al. 2015).

2.4 Discussion

2.4.1 HCO^+ and N_2H^+

The chemical effects of accretion bursts result from the change in temperature of the circumstellar gas and dust. In a low temperature environment, CO is frozen out on the dust grains and N_2H^+ is abundant in the cold regions where CO is frozen-out because CO reacts with and destroys N_2H^+. However, as the temperature increases on the grain mantles due to the accretion burst, CO begins to evaporate. The CO evaporation rate is independent of the gas density and is exponentially proportional to the temperature of the dust grains. Hence, the evaporation is effectively instantaneous. Consequently, N_2H^+ gets destroyed by proton exchange with the evaporating CO molecules forming HCO^+. This brings about a significant change on the radial abundance of these molecular species before and during bursts (Visser & Bergin 2012; Visser et al. 2015).

This effect can be seen in Figures 2.2 and 2.3. At the central region near the protostar, where the temperature increase is the highest, we see that HCO^+ is peaked whereas N_2H^+ is reduced. Instead, N_2H^+ is double-peaked surrounding the protostar position. These observations are in good agreement to the models of Visser & Bergin (2012). However, it is important to note that while the models of Visser & Bergin (2012) suggest that N_2H^+ should only be present outside R∼500 AU, outside the region of majority of HCO^+, we do see spatial overlap between HCO^+ and N_2H^+ lines. This is due to the longer destruction timescale of N_2H^+ compared to the instantaneous CO evaporation and the limited angular resolution provided by the SMA. The complete molecular destruction of N_2H^+ takes roughly 50 - 100 yr. Hence, there simply has not been enough time for the destruction of N_2H^+ in this region since the outburst in ∼2006. Furthermore, the resolution of the SMA emission is not quite high enough to fully resolve the region within which N_2H^+ is destroyed.

Once the accretion burst is over and the protostar enters its quiescent phase, the temperature on the grains begins to drop. The evaporated CO eventually does freeze out onto the dust grains. However, the freeze-out rate is significantly slower than the evaporation rate. The CO freeze-out is given by the equation,

$$\tau_{\rm fr} = 1 \times 10^4 \sqrt{\frac{10\ {\rm K}}{{\rm T_g}} \frac{10^6\ {\rm cm^{-3}}}{n({\rm H_2})}}, \tag{2.1}$$

and depends on the collision rate between molecules and the grains (Charnley et al. 2001). This means that for H_2 density of 10^6 cm^{-3} and gas temperature of 10 K, the freeze-out timescale of CO is 10^4 yr. Thus, even after protostar enters its quiescent phase, the effects of the outburst are apparent for quite some time, possibly explaining the extent of $C^{18}O$ emission in the envelopes around protostars (Jørgensen et al. 2015; Frimann et al. 2017). This has the effect that N_2H^+ could continue to be destroyed out to larger radii.

2.4.2 $C^{18}O$ signatures

Another molecular signature that can be used to observe the impact of an accretion burst is the extent of the $C^{18}O$ emission. Jørgensen et al. (2015) found out that an accretion burst increases the sublimation radius of CO around the protostar. This extends the emission radius of $C^{18}O$ from the low accretion, low-luminosity state, predicted by the models. Once the burst is over and the luminosity of the protostar returns to its steady-state, however, the $C^{18}O$ emission will still be extended due to the slower freeze-out timescale of CO. Using line radiative transfer calculations, the extent of $C^{18}O$ emission can be compared to the predicted emission radius given the current luminosity of HOPS 383. However, because of spatial filtering from another velocity component in the molecular cloud, the size of the $C^{18}O$

emitting region cannot be accurately measured.

2.5 Conclusion

We have presented an analysis of molecular line emission using the SMA in Subcompact and Extended configurations towards the protostar HOPS 383. The emission maps of N_2H^+ and HCO^+ clearly show the chemical signatures of the accretion burst, resulting from the change in temperature of the gas and dust surrounding the protostar.

The N_2H^+ is marginally double-peaked around the protostar, suggesting that it is being destroyed by reaction with the evaporating CO molecules, forming HCO^+. Given the short time since the outburst in 2006, we see spatial overlap between CO and N_2H^+, as the molecular destruction of N_2H^+ takes ~50 - 100 yr. The HCO^+ and $H^{13}CO^+$ emission is concentrated around the protostar position, as suggested by Visser & Bergin (2012), where N_2H^+ is reduced. Since the freeze-out of CO takes about 10^4 yr, N_2H^+ in the inner regions of the envelope should continue to react with CO to larger radii, significantly changing the radial abundances of these molecules.

Furthermore, we found H_2CO around the warm regions of HOPS 383, suggesting that it was frozen-out before the outburst. This could potentially serve as another tracer of an outburst in protostars but further observations around multiple systems undergoing outbursts are needed to better ascertain its plausibility. The $C^{18}O$ emitting region could not be measured accurately due to contamination by a foreground cloud with similar velocity range.

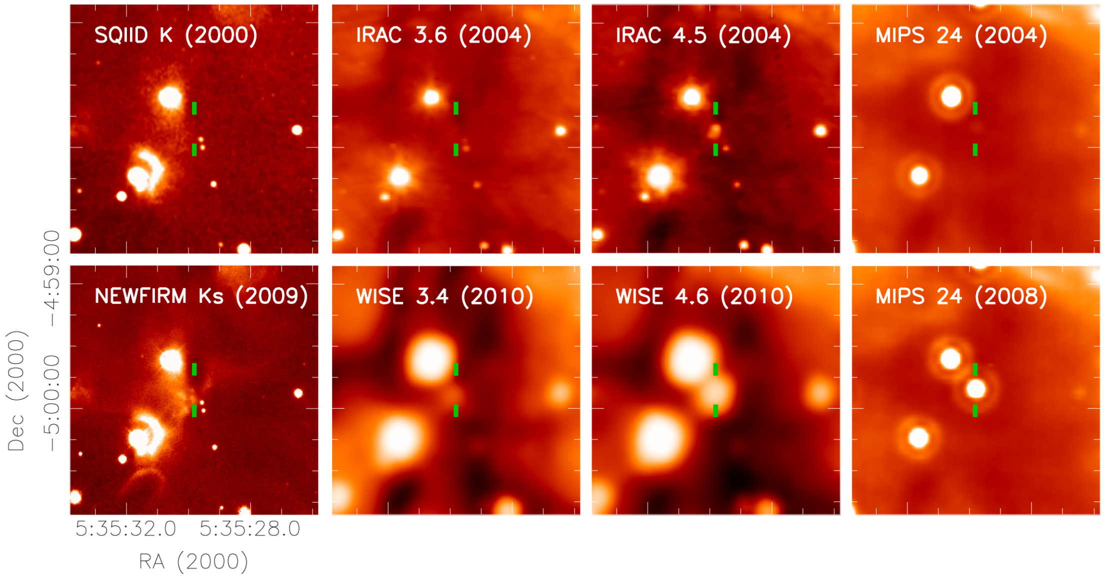

Fig. 2.1.—: Near- and mid-IR images of HOPS 383 before and after its outburst around 2006. The top row images show the pre-outburst imaging from SQIID and *Spitzer*. The bottom row images show post-outburst imaging from NEWFIRM, WISE, and *Spitzer*. The position of HOPS 383 is marked by the green dashes. This image was taken from Safron et al. (2015).

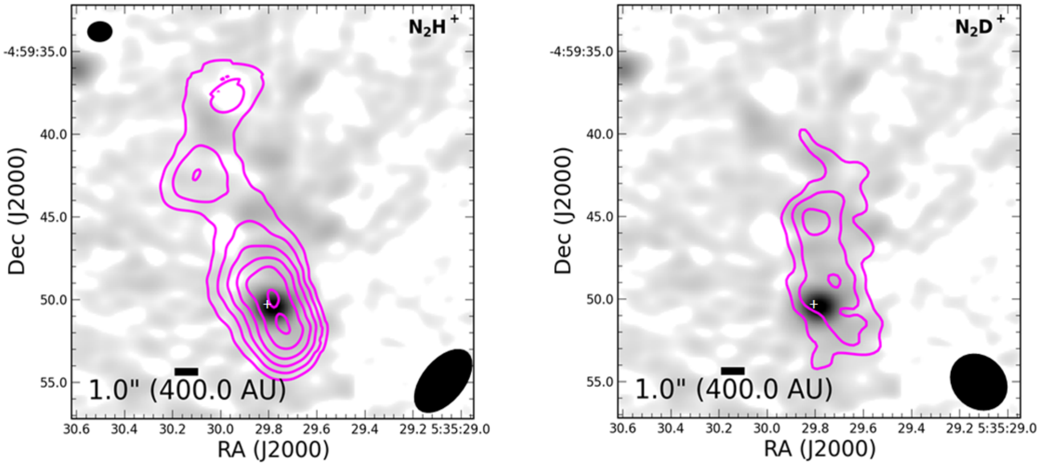

Fig. 2.2.—: Integrated intensity images from the combined Compact and Extended SMA observations of N_2H^+ ($J = 3 \rightarrow 2$) and N_2D^+ ($J = 3 \rightarrow 2$) overlaid on the continuum obtained from the combined Subcompact and Extended 1.3 mm SMA data. The contours start at 4σ with steps of 2σ for N_2H^+ with $\sigma \approx 0.34$ Jy beam^{-1} respectively and start at 3σ with steps of 1σ for N_2D^+ with $\sigma \approx 0.078$ Jy beam^{-1}. The beam size is $4\farcs3 \times 2\farcs5$ for N_2H^+ and $3\farcs5 \times 3\farcs0$ for N_2D^+. The background continuum beam size is $1\farcs5 \times 1\farcs2$ and is shown on the top left of the N_2H^+ image. The location of the protostar is given by the white cross.

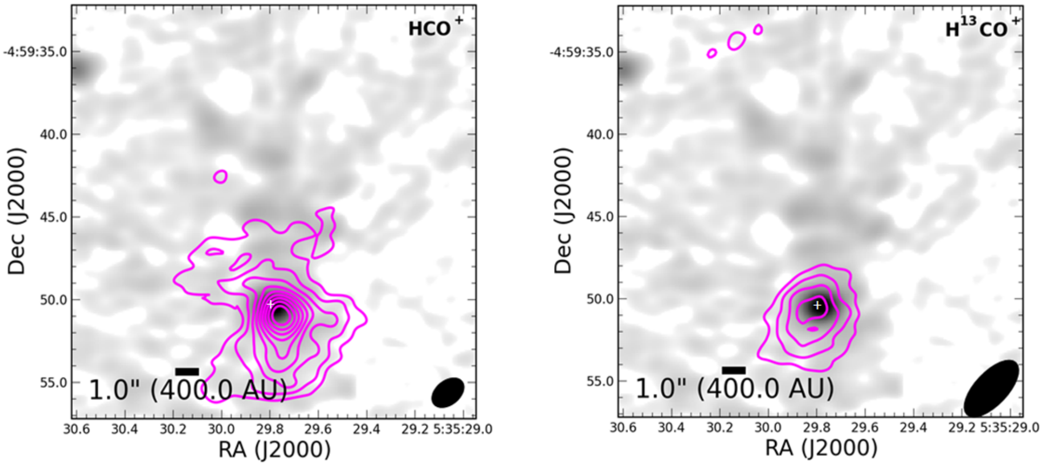

Fig. 2.3.—: Integrated intensity images from the combined Compact and Extended SMA observations of HCO$^+$ ($J = 3 \rightarrow 2$) and H^{13}CO$^+$ ($J = 3 \rightarrow 2$) overlaid on the continuum obtained from the combined Compact and Extended 1.3 mm SMA data. The contours start at 4σ with steps of 2σ for both HCO$^+$, and H^{13}CO$^+$ with $\sigma \approx 0.15$, and 0.095 Jy beam^{-1} respectively. The beam size is $2\farcs0 \times 1\farcs4$ for HCO$^+$ and $4\farcs1 \times 1\farcs9$ for H^{13}CO$^+$. The background continuum beam size is $1\farcs5 \times 1\farcs2$, the same as on Figure 2.2. The location of the protostar is given by the white cross.

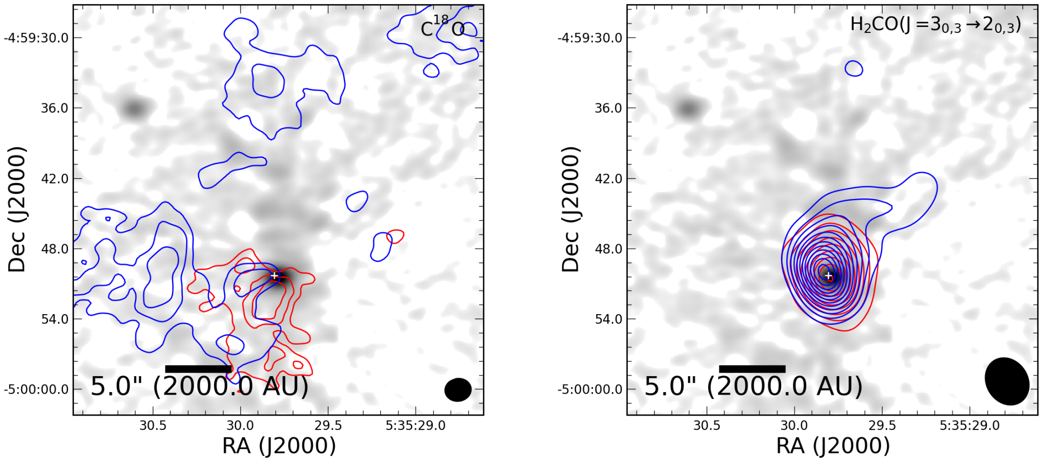

Fig. 2.4.—: HOPS 383 red- and blue-shifted integrated intensity map tracing the emission from $C^{18}O$ (*left*) and H_2CO (*right*) from the SMA observations overlaid on the continuum obtained from the combined Compact and Extended 1.3 mm SMA data. The $C^{18}O$ contours start at 4σ with steps of 2σ with $\sigma \approx 0.06$ Jy beam^{-1} and $\sigma \approx 0.10$ Jy beam^{-1} for the red- and blue-shifted emission, respectively. The H_2CO contours start at 4σ with steps of 2σ with $\sigma \approx 0.05$ Jy beam^{-1} and $\sigma \approx 0.03$ Jy beam^{-1} for the red- and blue-shifted emission, respectively. The beam size is $2\farcs2 \times 1\farcs9$ for $C^{18}O$ and $4\farcs2 \times 3\farcs5$ for H_2CO. The background continuum beam size is $1\farcs5 \times 1\farcs2$, the same as on Figure 2.2. The location of the protostar is given by the white cross.

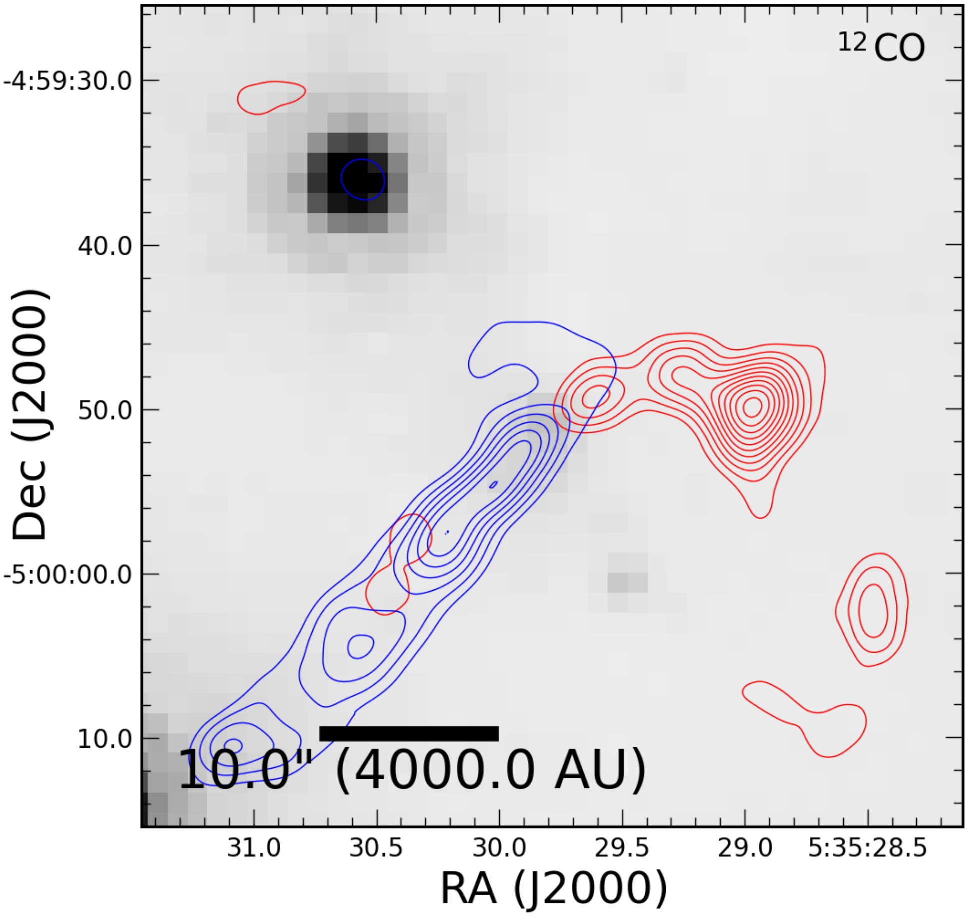

Fig. 2.5.—: HOPS 383 ^{12}CO red- and blue-shifted integrated intensity map tracing the outflow from the combined Subcompact and Extended SMA observations overlaid on the *Spitzer* image. The blue-shifted contours start at 5σ with steps of 2σ with $\sigma \approx 0.15$ Jy beam^{-1}. The red-shifted contours start at 4σ with steps of 1σ with $\sigma \approx 0.045$ Jy beam^{-1}.

Chapter 3

High Resolution Continuum Observation of the Youngest Outbursting Protostar HOPS 383

3.1 Introduction

A fundamental unknown in low-mass star formation is the process by which protostars accrete their mass, especially in their early phase. In particular, the youngest Class 0 and Class I protostars are surrounded by a protostellar disk which itself is deeply embedded in a thick, dense envelope, making it very difficult to directly observe the accretion process. Initially, it was thought that the accretion process was quasi-steady with roughly constant accretion rate throughout the protostellar phase (Shu 1994). However, observations of accretion bursts in FU Ori- and EX Lup-type objects provide growing evidence that accretion is episodic in nature, with many stochastic events of high accretion throughout the formation of a star (e.g. Herbig 1977; Reipurth 1989; Hartmann & Kenyon 1996; Greene et al. 2008). Observation of knots in outflows from YSOs (e.g. Dopita 1978; Reipurth 1989) also provide additional evidence for episodic accretion. Such periodically spaced knots in the outflow are thought to be driven by high accretion of material from its disk, indicative of episodic accretion (e.g. Pudritz et al. 2007; Shang et al. 2007, Arce et al. 2013; Plunkett et al. 2015).

Recently, a highly favored scenario that has come forward is that protostellar accretion proceeds in two co-existing phases (Kenyon & Hartmann 1995). Accretion from the protostellar disk primarily occurs in brief, powerful bursts of high accretion, followed by long periods of low accretion, whereas accretion from the envelope to the disk occurs in a fairly constant manner throughout the evolution. This scenario is able to explain both the low luminosities of young protostars (Dunham et al. 2010; Offner & McKee 2011) and the large spread in luminosities of protostars (Baraffe et al. 2009, 2012; Evans et al. 2009; Fischer et al. 2017).

The observational evidence for accretion bursts is quite strong (Audard et al. 2014). However, the nature and physical cause of episodic accretion are still unclear. The three main causes given for episodic accretion are (1) due to perturbations in the protostellar disk by close encounter with an external body, (2) due to gravitational instability (GI; Vorobyov & Basu 2005) and (3) magnetorotational instability (MRI; Armitage et al. 2001; also Gammie 1999) in a massive inner disk assembled by GI (Zhu et al. 2008). Although close encounters are a very real possibility in binary systems, highly increasing accretion rates for a short period (Bonnell & Bastien 1992), it fails to explain outbursts in isolated, single protostars.

On the other hand, GI mostly operates in the outer disk when the disk is sufficiently cold and massive to become gravitationally unstable and MRI operates mostly in the inner disk when sufficient ionization occurs due to sufficiently high temperature for the magnetic field to couple to the gas. Both of these instabilities transport angular momentum outwards, thereby allowing material to flow through the disk and accrete onto the protostar, giving rise to an outburst.

Episodic accretion has several important implications on the physical and chemical evolution of the protostellar disks. It is therefore very important to study such bursts at various stages of evolution for a complete picture of star formation process. The youngest protostar that was recently observed to undergo an outburst is HOPS 383, a class 0 protostar in Orion (Safron et al. 2015). HOPS 383 exhibits a unique opportunity to investigate the cause of accretion bursts and its importance for mass accretion in the very early stages of star formation. However, the highly embedded nature of HOPS 383 makes it impossible to study in optical wavelengths. The thermal dust emission and radio jets emitting free-free continuum are often the only way to probe the environment within a few hundred AU around a Class 0 protostar (e.g., Rodríguez 1997; Anglada et al. 1998). Hence, we make use of submillimeter and millimeter observations using radio telescopes to constrain the structure of the envelope and disk.

The study of the early phase of star formation in the last decade has gone through considerable breakthroughs with the advent of radio instruments such as the upgraded Karl G. Jansky Very Large Array (VLA) and the Atacama Large Millimeter/submillimeter Array (ALMA). The superior sensitivity and resolution of these instruments make it possible to resolve structures in <100 au scales, allowing us to study protostellar systems in great detail. These facilities have made it possible to observe protostars at different stages of their evolution which enables us to test the theories of star formation (Terebey et al. 1984; Shu et al. 1987) with greater fidelity than ever before.

In this chapter, I present continuum observations of HOPS 383, taken with ALMA and the VLA, as a follow-up after its outburst. I use the high resolution and sensitivity data to constrain the mass of the disk and use it to test the plausibility of GI as the cause of the outburst. The observations and data reduction are described in Section 3.2. The empirical results from the observations are presented in Section 3.3. The implications of our results are discussed in Section 3.4 and the conclusions are presented in Section 3.5.

3.2 Observation and Data Reduction

3.2.1 ALMA

HOPS 383 was observed on 2016 September 6 & 2017 July 19 with ALMA located in the Llano de Chajnantor, Chile in band 7 (0.87 mm) during Cycle 3 and 4 (Project code: 2015.1.00041.S.) as part of the VLA/ALMA Nascent Disk and Multiplicity (VANDAM) Survey. The total on source time was ∼54 seconds. The baselines covered ranged from 15 m to 3697 m.

The correlator setup for the 0.87 mm observations correlator consisted of two of the basebands set to low spectral resolution 1.875 GHz continuum windows of 31.25 MHz channels. These basebands were centered at 333 GHz and 344 GHz. The third baseband was centered on ^{12}CO ($J = 3 \rightarrow 2$) at 345.8 GHz with a 937.5 MHz spectral window (0.489 km s^{-1} channels) and the last baseband was centered on ^{13}CO ($J = 3 \rightarrow 2$) at 330.6 GHz with a 234.375 MHz (0.24 km/s channels) spectral window, although we were unable to detect it. The bandpass calibrator in the first 2016 observation was J0510+1800, during the second 2016 observation J0510+1800 was used, and the 2017 observation used J0522-3627 as the bandpass calibrator. J0510+1800, J0541-0541, and J0750+1231 were used as the absolute flux calibrators for the respective observations and J0541-0541 was used as the complex gain calibrator for all the observations.

To account for the variation of the quasar J0510+1800 used for flux calibration, the data were reduced manually by the Dutch Allegro ARC Node. All further processing was done using *CASA* version 4.7.2 (McMullin et al. 2007). The spectral line data was imaged by subtracting the continuum data, using the task *clean* with a velocity resolution of 1 km s^{-1} for ^{12}CO, and 0.5 km s^{-1} for ^{13}CO. The signal-to-noise ratio of the continuum images was improved by performing self-calibration on the continuum and also applying these solutions to the spectral line data. The final continuum image was produced using Briggs weighting with a robust parameter of 0.5, providing a balance between sensitivity and resolution. This resulted in a synthesized beam of $0\farcs11 \times 0\farcs10$ and RMS noise of 0.28 mJy beam^{-1}.

3.2.2 VLA

HOPS 383 was observed with VLA located in San Agustin Plains, New Mexico, USA in the C-array on 2016 February 16 and in A-array on 2016 November 16. Our observations obtained lower-resolution ($\sim 0\farcs7$) C-array data and high-resolution ($0\farcs065$) A-array data for HOPS 383. During each observation, 26 antennas were operating and the entire observation lasted 2.5 hours. The observations were conducted with Ka-band receivers and three-bit correlator mode with one 4 GHz baseband centered at 36.9 GHz (8.1 mm) and the second 4 GHz baseband was centered at 29 GHz (1.05 cm). We used 3C48 (J0137+3309), 3C84 (J0319+4130), and J0541-0541 as the bandpass, absolute flux, and complex gain calibrators respectively. To reduce the effect of rapid atmospheric phase variations in high-frequency observations, the observations were made in fast-switching mode and the total time on source was ∼64 minutes.

The data were reduced using the scripted version of the VLA pipeline in *CASA* 4.4.0. The continuum was imaged using the *clean* task in *CASA* 4.5.1 using Natural weighting, multi-frequency synthesis with *nterms=2* across both basebands. The final image has an RMS noise of 7.16 μJy beam^{-1} and a synthesized beam of $0\farcs08\times0\farcs07$ (32 AU × 28 AU).

3.3 Results

3.3.1 Continuum

We show the continuum images of HOPS 383 obtained from the ALMA at 870 μm and the VLA at 9 mm in Figure 3.1. The images show a very strong detection at these wavelengths, with the ALMA images showing that the dust continuum emission from HOPS 383 is resolved with its major axis oriented perpendicular to the outflow direction (Figure 2.5). Thus, the resolved emission orthogonal to the outflow is suggestive of the continuum emission tracing a resolved protostellar disk. The VLA image is more compact but is also resolved as the spatial extent of the continuum is at least 1.1 × the size of the FWHM of the beam. Also, we observe a decrease in flux at the longest baselines from the VLA visibility profile (see Chapter 4), indicating that we have resolved the continuum.

The integrated flux density of HOPS 383 at 870 μm is 157.75 ± 3.2 mJy with peak flux density value of 47 ± 0.7 mJy/beam. Likewise, the integrated flux density for the 8 mm wavelength data from the VLA is 411 ± 17 μJy with peak flux density value of 290 ± 7 μJy/beam. We also obtained the integrated flux density of HOPS 383 obtained from the SMA in 0.85 mm, 1.1 mm and 1.3 mm in subcompact configuration and 1.1 mm and 1.3 mm in Extended configuration. The SMA continuum is not as well resolved as the ALMA and the VLA and we only use it as the background of Figures 2.2, 2.3, and 2.4. However, we include the obtained integrated flux density from the various SMA observations along with the ALMA and the VLA observations in Table 3.1.

3.3.2 Millimeter to Centimeter Spectrum

Using the data from the ALMA and the VLA, we add new data to extend the Spectral Energy Distribution (SED) of HOPS 383 to millimeter and centimeter wavelengths. Figure 3.3 shows the spectrum of the protostar at the millimeter wavelengths along with a few centimeter wavelengths data from the VLA archive reported by Galvàn-Madrid et al. (2015). From the archival data, we averaged the 2014 data and discarded the ones with upper-limits for flux (see Table 1, Galvàn-Madrid et al. 2015). HOPS 383 is not at the phase center of these archival data but lies within the field of view.

Figure 3.3 shows that the millimeter wavelength is dominated by the dust emission while the longer wavelengths are dominated by the free-free emission. In the optically thin centimeter region, the free-free emission spectrum is almost flat. The 8 mm to 1 cm data falls in the transition from dust to free-free emission. We use the *curve_fit* from Python's *scipy* library to fit the free-free emission power law to the longer wavelength data and subtract the extrapolated contribution from the free-free emission to the flux densities on the 8 mm to 1 cm data. We then fit another power law for the dust emission for the millimeter data. The free-free contribution to the 8 mm, 9 mm, and 1 cm data is found to be ∼0.232 mJy, ∼0.234 mJy, and ∼0.237 mJy, respectively. From the SED, we get the power law as $F_{\lambda,\mathrm{dust}} = (0.17 \pm 0.08)\lambda^{-2.85\pm0.05}$ mJy and $F_{\lambda,\mathrm{ff}} = (0.24 \pm 0.09)\lambda^{0.09\pm0.27}$ mJy.

3.3.3 Disk Mass

The resolved dust continuum emission from the VLA and the ALMA can be used to calculate the mass of the total disk structure surrounding HOPS 383. Assuming an isothermal disk, well-mixed gas and dust, and optically thin emission, the disk mass is given by,

$$M_{\mathrm{dust}} = \frac{D^2 F_\lambda}{\kappa_\lambda B_\lambda(T_{\mathrm{dust}})}, \tag{3.1}$$

where D is the distance to the source (∼400 pc), T_{dust} is the dust temperature, F_λ is the flux density observed at λ, κ_λ is the dust opacity, and B_λ is the Planck function at the wavelength, λ. We take $\kappa_{1.3\ \mathrm{mm}} = 0.899\ \mathrm{cm^2 g^{-1}}$ for thin ice mantles from dust opacity models of Ossenkopf & Henning (1994) and scale the opacities to the wavelength of ALMA and VLA using the equation,

$$\kappa_\lambda = \kappa_{1.3\ \mathrm{mm}} \times \left(\frac{1.3\ \mathrm{mm}}{\lambda}\right)^\beta, \tag{3.2}$$

where β is the dust opacity spectral index. For a typical protostar with low luminosity (~1 - 3 $L_\odot$), T_{dust} is assumed to be constant at 30 K, compatible with protostar disk estimates on ~100 au scales (Whitney et al. 2003). We can thus scale the average T_{dust} for HOPS 383 using $(L/L_\odot)^{0.25}$, as expected from thermal equilibrium. This gives us an average temperature of ~50 K for $L_{bol} = 7.8\ L_\odot$, which we use as a high temperature estimate for HOPS 383. Assuming canonical ISM dust to gas mass ratio of 1:100 (Bohlin et al. 1978), we multiply the resulting dust mass by 100 to get the total disk mass.

The continuum flux density from the ALMA at 870 μm has a flux density of 158 ± 3.2 mJy. Assuming $\beta \sim 1.78$, which is indicative of young, embedded cores, we obtain disk mass of 0.082 $M_\odot$ and 0.043 $M_\odot$ for $T_{\mathrm{dust}} = 30$ K and $T_{\mathrm{dust}} = 50$ K, respectively. Since HOPS 383 is a young protostar, the dust emission may not be optically thin at 0.87 mm, thus, the disk masses are likely lower limits for their respective temperatures.

The continuum flux density from the VLA at 9 mm has a flux density of 411 ± 1.7 μJy. Assuming $\beta \sim 1$ here, which yields more consistent results between 1.3 mm and 1 cm (Tobin et al. 2016; Tychoniec et al. 2018), we obtain total disk mass of 0.25 $M_\odot$ and 0.15 $M_\odot$ for $T_{\mathrm{dust}} = 30$ K and $T_{\mathrm{dust}} = 50$ K, respectively. Subtracting the contribution of the free-free emission at 9 mm (0.234 mJy), we get total disk mass of 0.11 $M_\odot$ and 0.063 $M_\odot$ for $T_{\rm dust}$ = 30 K and $T_{\rm dust}$ = 50 K, respectively. The dust emission at 9 mm is likely more optically thin than the dust emission at 870 μm, which is why it is tracing higher dust mass. Hence, assuming we have the correct opacity, we measure larger VLA masses than the ALMA masses.

3.4 Discussion

3.4.1 Flux Derived Toomre Q

The observed flux of the ALMA gives us a disk masses of 0.082 $M_\odot$ (T_{dust} = 30 K) and 0.043 $M_\odot$ (T_{dust} = 50 K). Similarly, from the VLA fluxes, we have disk masses of 0.25 $M_\odot$ (T_{dust} = 30 K) and 0.15 $M_\odot$ (T_{dust} = 30 K). Removing the free-free contribution to these fluxes gives us masses of 0.11 $M_\odot$ and 0.063 $M_\odot$, respectively. With these masses we can calculate Toomre's Q parameter to assess the stability of the rotating disk of HOPS 383 against gravitational collapse. It calculates the ratio of rotational shear force and thermal pressure to the self-gravity of the disk,

$$Q = \frac{c_s \Omega}{\pi G \Sigma}, \tag{3.3}$$

where c_s is the sound speed, Ω is the differential rotation value of a Keplerian disk, G is the gravitational constant, and Σ is the disk surface density. The stability of the disk requires $Q > 1$ and $Q < 1$ indicates that the disk is gravitationally unstable and may be prone to fragmentation.

We can rewrite this equation (Kratter & Lodato 2016; Tobin et al. 2016) in the form,

$$Q \approx 2\frac{M_* H}{M_d R}, \tag{3.4}$$

where, M_* is the mass of the protostar, $H = c_s/\Omega$, M_d is the mass of the disk and r is the radius of the disk at which the c_s is measured. Using a typical protostar mass of 0.5 $M_\odot$ (Kenyon & Hartmann 1995), we find that $Q \approx 2.83$ and 1.15 for $M_{\rm disk} = 0.043 M_\odot$ and 0.082 $M_\odot$, respectively for the disk masses obtained from ALMA flux density. Thus, Q is currently > 1 if we take T = 50 K, and the disk is most likely being stabilized during the outburst, but prior to the outburst when the disk was more likely ∼30 K, Q would be lower and closer to instability by a factor of $(50/30)^{0.5} \approx 1.29$. Furthermore, with the likely underestimate of disk mass, Q would be lower as well. Thus, while we cannot absolutely confirm that the disk is or was unstable, the disk appears to have sufficient mass to make gravitational instability a very plausible outburst mechanism for HOPS 383.

On the other hand, if the VLA masses we obtained are correct; then $Q \approx 1.93$ and 0.87 for $M_{\rm disk} = 0.063 M_\odot$ and 0.11 $M_\odot$, respectively. The lower temperature prior to the outburst further justifies GI as the cause of the outburst. Although we use a typical protostar mass of 0.5 $M_\odot$ for HOPS 383, this might be an overestimate. The extremely young age of HOPS 383 implies that the protostar mass might be less massive. If this is true, then Q will also be lower and closer to 1.

3.5 Conclusion

We report ALMA and VLA observations of the youngest known outbursting protostar, HOPS 383 with ∼40 au resolution. The ALMA observations resolve the dust continuum at 870 μm, revealing a protostellar disk orthogonal to the outflow. The VLA observation at 9 mm is resolved but is much more compact than the ALMA observations. We use the obtained continuum emission to extend the spectrum of HOPS 383 to millimeter wavelengths and connect it to the centimeter data reported by Galvàn-Madrid et al. (2015).

We estimate the disk mass from the ALMA and the VLA continuum to be $\sim$0.043 $M_\odot$ and $\sim$0.15 $M_\odot$, respectively for dust temperature of 50 K after the outburst, as indicated by its luminosity of 7.8 $L_\odot$. Using the ALMA disk mass and a typical protostar mass of 0.5 $M_\odot$, we calculate Toomre's Q, finding a disk becoming gravitationally stabilized with $Q > 1$. Prior to the outburst, however, with lower temperature and luminosity, the disk mass would be larger, making it likely to be gravitationally unstable. Multiple future high-resolution millimeter imagery of the system can help constrain the disk properties with greater precision to test the GI as well as MRI as the cause of the outburst.

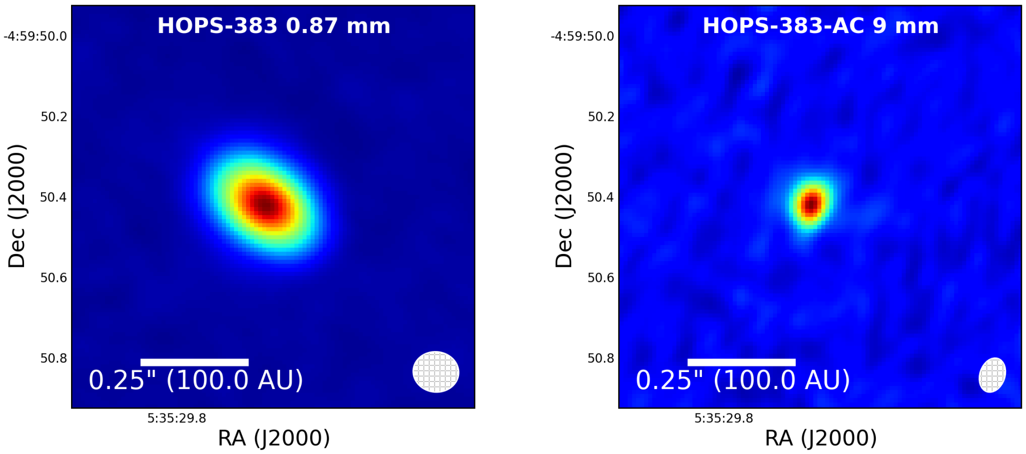

Fig. 3.1.—: HOPS 383 continuum images at 870 μm (*left*) and 9 mm (*right*) observed with the ALMA (Cycle 3 & 4), and the VLA respectively. The beam size in each figure is $0\farcs11 \times 0\farcs10$ and $0\farcs09 \times 0\farcs06$ at 870 μm and 9 mm respectively.

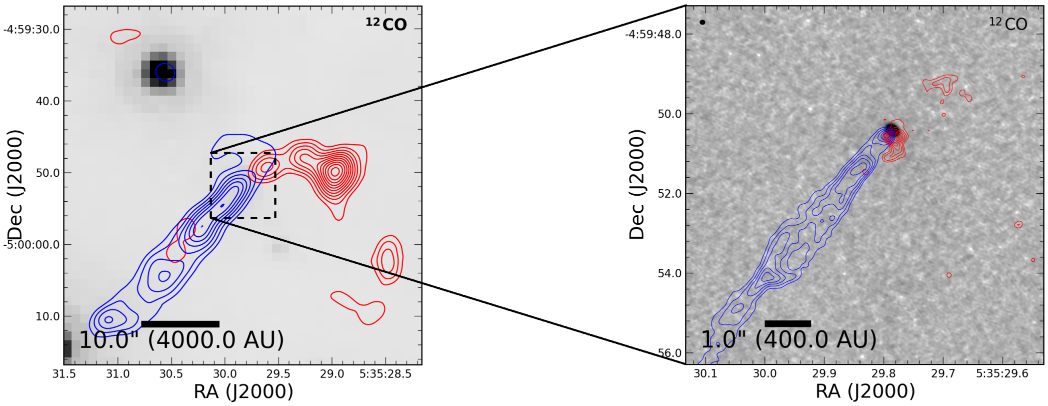

Fig. 3.2.—: Left: Integrated emission map of ^{12}CO obtained from the SMA as shown in Figure 2.5. Right: Higher resolution plot of the ^{12}CO red- and blueshifted integrated intensity map tracing the outflow from the ALMA 870 μm observations overlaid on the continuum image from ALMA. The blue-shifted contours start at 5σ with steps of 2σ with $\sigma \approx 0.15$ Jy beam^{-1}. The redshifted contours start at 4σ with steps of 1σ with $\sigma \approx 0.045$ Jy beam^{-1}. The spatial region covered by the ALMA plot is shown by the dashed square in the SMA figure.

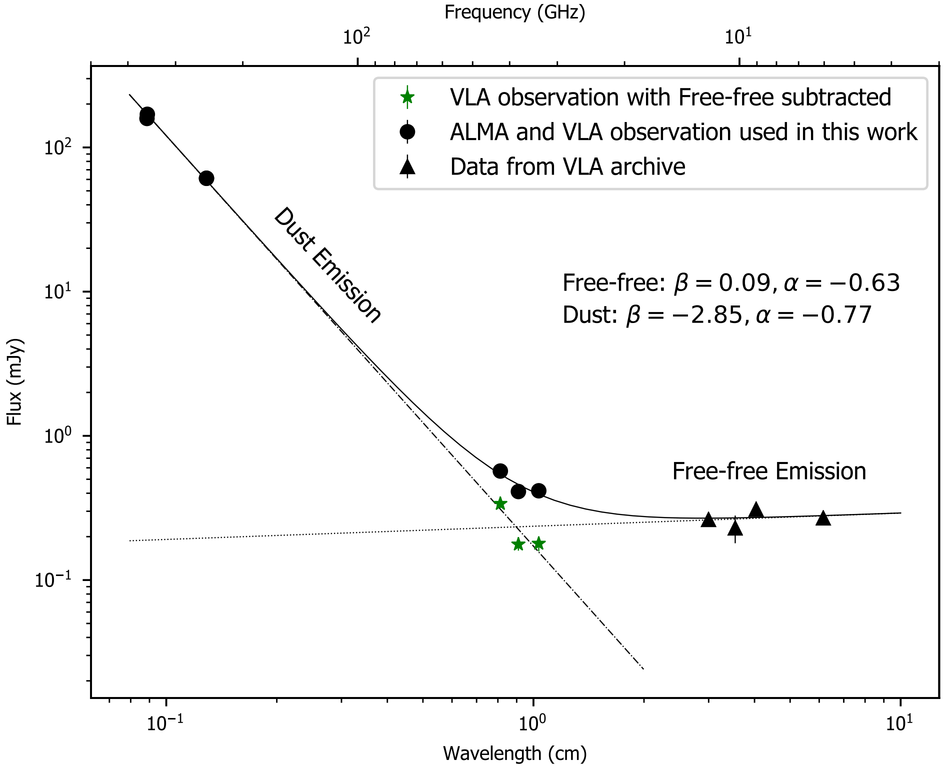

Fig. 3.3.—: The observed millimeter to centimeter spectrum of HOPS 383. The black circles are the data from the ALMA and the VLA used in this work. The black triangles are data taken from the VLA archive as shown in Table 1 of Galvàn-Madrid et al. (2015). We exclude the points with only upper limits and flux data before the outburst. We also only include the average of all the flux data for the 10 GHz archival data. The green stars represent the VLA data used in this work with the extrapolated free-free emission subtracted.

Table 3.1:: Integrated flux density of HOPS 383 obtained from various sub-millimeter to millimeter wavelength.

Wavelength (mm)	Flux Density (mJy)	Peak Flux (mJy bm^{-1})	RMS (mJy)	Instrument	Configuration	Beam Size (″)
0.85	323.46 ± 12.7	237.36	5.44	SMA	Subcompact	2″.92 × 2″.78
0.87	157.75 ± 3.2	47.11	0.72	ALMA	-	0″.11 × 0″.10
1.1	147.74 ± 12.2	76.73	3.4	SMA	Subcompact	6″.07 × 2″.93
1.1	172.47 ± 8.9	131.72	3.93	SMA	Subcompact w/SWARM	5″.94 × 2″.81
1.3	136.63 ± 6.7	90.81	2.70	SMA	Subcompact	3″.77 × 3″.67
1.3	75.72 ± 3.7	68.88	2.0	SMA	Extended	1″.46 × 1″.06
9	0.411 ± 0.017	0.290	0.007	VLA	A+C combined	0″.09 × 0″.06

Chapter 4

Properties of Protostellar Disk and Envelope of HOPS 383 Using Radiative Transfer Modeling

4.1 Introduction

The star formation process begins with the collapse of gas and dust to form a protostar. At the earliest stage of star formation, the Class 0 phase (André et al. 1993), newborn protostars are deeply embedded by their natal envelopes. As the collapse proceeds, the initial angular momentum of the protostellar cloud naturally deposits most of the material onto a rotationally supported disk. There has been observational evidence for disks around Class 0 protostars (e.g. Tobin et al. 2012; Murillo et al. 2013; Codella et al. 2014, Lee et al. 2014; Yen et al. 2015, 2017), suggesting such disks form very early around protostars. The formation of such a disk is a crucial point of stellar evolution as it regulates the accretion of material to the protostar and will ultimately serve as the site of planet formation. Furthermore, sufficiently massive disks may become gravitationally unstable, leading to accretion bursts (Vorobyov & Basu 2006).

To understand how disks can become gravitationally unstable, it is necessary to constrain the general properties of the disks such as their mass, temperature distribution, and radii. Some of these properties can be extracted from the observed dust emission from the disks. However, the highly embedded Class 0 phase can only be observed in submillimeter and millimeter wavelengths, where the emission of the envelope is entangled with that of the disk (André et al. 1993; Dunham et al. 2014). Moreover, dense regions of the disk at small radii can be optically thick, preventing the flux density from tracing all mass in this region. Consequently, the properties of disks of early phase protostars have not been characterized for a broad sample. Radiative transfer modeling can overcome these obstacles, disentangling the flux from the envelope and the disk and unambiguously resolve the properties of protostellar disks.

Radiative transfer modeling has primarily been used to match the SEDs or the millimeter emission of YSOs. Although these models can constrain the distribution of the material around the protostars (e.g. Adams et al. 1987; Kenyon et al. 1993; Robitaille et al. 2007), they are subject to degeneracies. The same SED or millimeter emission can be explained by different models. For example, it is difficult to distinguish between a flattened, disk-like envelope (Ulrich 1976; Terebey et al. 1984) and flared, edge-on disk (Chiang et al. 1999) from just the SED. Similarly, the same sample continuum of Class 0 protostars could be explained by the presence of disks between 0.002 and 0.5 $M_\odot$ (Jørgensen et al. 2009) and using an envelope with non-uniform density structure without a disk (Chiang et al. 2008). These degeneracies can be resolved by modeling multi-wavelength submillimeter/millimeter visibilities and SEDs from near-IR to millimeter simultaneously. This helps to provide tighter constraints on the properties of the disk and the envelope, in addition to breaking the degeneracies. Such models have been used to better constrain the structure of the protostellar systems than by modeling a single data set (e.g. Eisner et al. 2005; Eisner 2012;

Sheehan & Eisner 2014).

In this chapter, I present the radiative transfer modeling of the disk around the outbursting Class 0 protostar HOPS 383 to constrain the properties of its disk and its envelope. I use the continuum data from ALMA and the VLA reported in Chapter 3 and the broadband SED of HOPS 383 after its outburst, taken from Safron et al. (2015) to create a model of HOPS 383 using multiple data sets. The data used in the SED are listed in Table 4.2. The results of the modeling should provide more explicit insight on the stability of the disk and the cause of the outburst. Section 4.2 presents a detailed overview of the procedure used in our models. The results from the models are presented in Section 4.3. The implications of the results are given in Section 4.4 and the conclusions are presented in Section 4.5.

4.2 Model Overview

To understand the cause of the outburst and study the features of HOPS 383 in detail, we use 3D Monte Carlo radiative transfer modeling to create synthetic models of the protostar that match the visibilities from the VLA and/or ALMA and the SED of HOPS 383. We followed the modeling procedure of Sheehan & Eisner (2014) and Sheehan & Eisner (2017). The models have a protostar at the center, surrounded by a circumstellar disk and an envelope with an outflow cavity. The different components and the free parameters of the models, along with a brief outline of the modeling technique are described below.

4.2.1 Protostar

Our models include a central protostar with a temperature of 4000 K, representative of a general low mass star in the pre-main sequence phase. Since the $\mathrm{T_{eff}}$ of Class 0 YSOs such as HOPS 383 have not been classified, this is a reasonable estimate to use for the models. The luminosity, L_*, which includes stellar luminosity and accretion luminosity, is left as a free parameter in all our models.

4.2.2 Protostellar Disk

The protostellar disk model uses the standard density profile of a flared exponentially-tapered accretion disk (e.g. Lynden-Bell & Pringle 1974),

$$\rho = \rho_0 \left(\frac{R}{R_0} \right)^{-\alpha} exp\left(-\frac{1}{2} \left[\frac{z}{h(R)} \right]^2 \right), \tag{4.1}$$

$$h(R) = h_0 \left(\frac{R}{1\ \mathrm{au}} \right)^{\beta}. \tag{4.2}$$

Here, R and z are the usual variables in cylindrical coordinates. ρ_0 is the density of the midplane at a radius of $R_0 = 1$ AU. $h(R)$ is the disk scale height, and h_0 is the scale height at 1 AU. We truncate the disk at a specific inner radius, R_{in}, which is left as a free paramater.

We define the surface density profile as,

$$\Sigma = \Sigma_0 \left(\frac{R}{R_0} \right)^{-\gamma}. \tag{4.3}$$

Here, γ is the surface density power-law exponent given by $\gamma = \alpha - \beta$, and β is scale height power law. The disk is truncated at a specific inner radius, R_{in} in all models. For the outer radius of the disk, R_{disk}, we run both models with R_{disk} truncated at a specific outer radius and with R_{disk} exponentially tapered. Similarly, in the models we treat the disk mass, M_{disk}, h_0, γ, β as free parameters as well.

4.2.3 Envelope

A Class 0 protostar such as HOPS 383 is embedded in an envelope extending beyond the protostellar disk. We model the envelope using the solution for the density profile of a rotating collapsing envelope found by Ulrich (1976),

$$\rho = \frac{\dot{M}}{4\pi(GM_*r^3)^{\frac{1}{2}}}\left(1+\frac{\mu}{\mu_0}\right)^{-\frac{1}{2}}\left(\frac{\mu}{\mu_0}+2\mu_0^2\frac{R_c}{r}\right)^{-1}. \tag{4.4}$$

Here M_* is the mass of the protostar, $\dot{M}$ is the mass infall rate from envelope to disk and R_c is the critical radius inside which the envelope starts to flatten and material starts to accrete onto the disk (Ulrich 1976; Terebey et al. 1984). In our model $R_c = R_{disk}$, $\mu = cos\theta$, and r and θ are the usual variables in spherical coordinates. $\mu_0 = cos\theta_0$ is the initial angle of the infalling material (Ulrich 1976). The envelope in our models is truncated at the same inner radius, R_{in}, as the disk and an outer radius, R_{env}. The envelope mass M_{env} and R_{env} are left as free parameters.

Our envelope models have an outflow cavity, whose location is determined by,

$$z > 1\ \mathrm{au} + r^{\xi} \tag{4.5}$$

Inside the outflow cavity, the envelope density is reduced by the scaling factor for the density, f_{cav}. ξ is related to the outflow cavity opening angle by the relation,

$$\text{Opening angle} = 2\tan^{-1}\left(R_{\mathrm{env}}^{(1/\xi-1)}\right) \tag{4.6}$$

and is left as a free parameter in all our models along with f_{cav}.

4.2.4 Dust

Our disk models for modeling the ALMA visibilities use the same dust opacities as Sheehan & Eisner (2014) and have similar dust grain sizes to the icy dust grains from Ossenkopf & Henning (1994). The dust model formula is taken from Pollack et al. (1994) and is appropriately adjusted to match the dense protostellar core from Ossenkopf & Henning (1994). The dust grain models consist of 40% silicate, 30% organics, and 30% water ice.

The dust in VLA disk models is taken from Woitke et al. (2016). The dust in our models follow a power-law grain size distribution with $n \propto a^{-p}$ with $p = 2.5$ - 4.5, based on $p = 3.5$ given by Mathis et al. (1977), where a is the dust grain size. The minimum grain size is assumed to be 0.005 μm for all opacities. We use maximum dust grain size of 1 μm for the dust in the envelope which is the same value as the interstellar medium. However, in the disk, the maximum size of the dust is left as a free parameter.

4.2.5 Radiative Transfer Codes

We use RADMC-3D (Dullemond 2012) for the continuum modeling and calculate the temperature throughout the density structure of the disk. The results are then used to produce synthetic observations of HOPS 383 to simultaneously fit the 0.87 mm visibilities or both the 0.87 mm and 8 mm visibilities plus the SED using Markov Chain Monte Carlo (MCMC) approach using the emcee code (Foreman-Mackey 2013). Once we have the temperature and the density, the synthetic SEDs and millimeter images are produced using ray tracing in RADMC-3D. The synthetic visibilities are then created using Fourier-transform on the synthetic millimeter images.

The MCMC walkers use Bayesian statistics to move through parameter space and reach a steady-state to provide estimates on the best-fit value for each of the free parameters. They aim to maximize the χ^2 of the model in log-space. We use the weighted sum of the χ^2 values of visibilities and the SED,

$$X^2 = w_{\mathrm{vis}}\chi^2_{\mathrm{vis}} + w_{\mathrm{SED}}\chi^2_{\mathrm{SED}} \tag{4.7}$$

where w is the weight of each data set. Our fits use $w_{\mathrm{vis}} = 0.5$ and $w_{\mathrm{SED}} = 1$ for both the ALMA only and the ALMA+VLA models, which we empirically determined to fit both data sets simultaneously. The walkers converge towards the regions of parameter space which fit the data well. The best-fit value is considered as the median position of the walkers once it has reached a steady-state and the parameter changes marginally over a large number of steps, i.e. the best fit values of the parameters remain more or less constant for $\sim$ 150 - 200 steps. The 1σ value around the median containing $\sim$68% of the walkers is considered as the uncertainty on the parameters.

We also leave the viewing angle parameters, inclination of the system (i) and position angle (p.a.) as free parameters in our models. We use Gaussian fits to the data to determine the offsets for the source and center the data accordingly. A summary of all the parameters used in the models is given in Table 4.1.

4.2.6 Model Fitting

In this paper, we fit models to the visibilities from the ALMA, and combined visibilities from the ALMA and the VLA to find the best fitting models of the continuum from HOPS 383. We do not include the visibility data from the SMA due to their lower signal-to-noise. The emcee code uses MPI to spread the model calculations to a large number of cores, significantly speeding up the computation of the models.

We model two different types of disks for both the ALMA and the combined ALMA+VLA models: i) where the disk is truncated at its critical radius and ii) where the disk exponentially tapers off to the envelope. It is still unclear if either disk type is better suited than the other for reproducing the observations. We want to verify any clear differences in the model results due to the difference in disk types. The ALMA only models use the Pollack et al. (1994) dust opacities.

However, using the Pollack et al. (1994) opacities on the combined ALMA+VLA required the disk mass to be unusually high (~1 $M_\odot$). Considering this to be unrealistic, we use the new opacities given by (Woitke et al. 2016) which have intrinsically higher opacity at longer wavelength providing more realistic disk masses.

4.3 Results

Our continuum dust models simultaneously reproduce the visibilities and the broadband SED for HOPS 383. We list the best-fitting parameter values for our disk models of HOPS 383 in Table 4.3, and show the different models compared with the data in Figures 4.1, 4.2, 4.3, and 4.4. It is important to note that the models only directly constrain the dust masses in the disk and envelope masses listed on Table 4.3. We assume a standard dust-to-gas ratio of 1:100. Thus the actual values constrained by the models are a factor of 100 lower than the ones given on the table. We discuss the results of our models below.

4.3.1 HOPS 383 ALMA Model

The ALMA only models appear to have very similar, massive envelopes with radii over ~7300 au and mass ~2.5 $M_\odot$. They also have similar luminosities of ~11 $L_\odot$. The truncated model has a protostellar disk mass of 0.1 $M_\odot$ which is 1.6 times more massive than the tapered model of 0.07 $M_\odot$. Both models independently get the same inclination, $i \approx 51°$ and position angle, $P.A. \approx 49°$. R_{disk} for the tapered model is smaller than the truncated model, which explains some of the lower mass. In both cases, the source is surrounded by a compact disk which is embedded within a large envelope which is over 25 times more massive than the disk.

Previous observations of HOPS 383 were mostly in infrared and had very few observations at millimeter wavelengths. The source was modeled by Safron et al. (2015) using *Spitzer*, *Herschel*, and APEX photometry, who found luminosities of $6\ L_\odot < L < 14\ L_\odot$, and $41^\circ < i < 63^\circ$. Our results are in good agreement with their findings.

4.3.2 HOPS 383 ALMA+VLA Model

The ALMA+VLA models results find a similar, massive disk of $M > 0.2\ M_\odot$ for both the truncated and the tapered cases. However, the disk radius is very different compared to the R_{disk} of the truncated model, which is about 3 times larger than the tapered model. They have very low-mass envelopes compared to their ALMA only counterparts with $M_{env} = 0.15\ M_\odot$ and $0.08\ M_\odot$ for the truncated and the tapered model, respectively. The luminosities are also fairly low with $\sim 4.0\ L_\odot$ for both models. The source appears to be less embedded than the ALMA only models with the disk being much more massive than the envelope. Also, comparing with the models by Safron et al. (2015), our models have lower luminosities.

Our models are not able to fully reproduce the visibilities from the VLA, without sacrificing the fit for the SED. This can be seen in the best-fit model of the VLA in Figures 4.3 and 4.4, where the SED fit appears worse visually. The fitting to the visibility data from the VLA also does not account for a contribution from the free-free emission that was calculated in Subsection 3.3.2. This mostly affects the fit to the baselines longer than 1000 kλ since dust dominates on larger scales. This is probably why there is a small excess of emission in the longer baselines, and the points do not go to 0 like the ALMA visibilities (Figures 4.3, 4.4). This excess could also in part explain why the VLA models arrive at such a higher mass.

4.4 Discussion

4.4.1 Key Parameter Differences From Models

Except for the ALMA tapered model, all other models have positive γ, i.e. decreasing surface density to longer radii, as expected. The negative γ for the ALMA tapered model can be attributed to the optically thick dust emission at 870 μm, which makes it difficult to trace γ very well. The emission at 8 mm is more optically thin and traces the dust in the disk more closely than at 870 μm.

A curious result of our models is the lower luminosity and significantly higher disk mass of ALMA+VLA models compared to the ALMA only models. Since the luminosities are derived mostly from the SED, it is surprising that the models have such different values. This result could be because higher luminosities of the ALMA only models might make the disk too bright for the VLA models. Similarly, the higher disk mass of the ALMA+VLA models could result from the 8 mm emission tracing the dust as well as the free-free emission in the disk that is more optically thin compared to the 870 μm emission.

The disk radius follows a similar pattern across the models, the tapered models have lower disk radii than the truncated models. It is difficult to properly define the disk radii for tapered models as the disk does not end at the critical radii, R_c, like in the truncated models. Instead, at R_c density of the disk starts to fall-off exponentially. Since the emission is likely optically thick, adding much more mass in the disk does not make it any brighter at short λ (i.e., 870 μm). So we can have a very massive disk with a small R_c where the disk density starts to fall-off, but it can still appear well-resolved out to the longer radii in the truncated models. For this reason, it is difficult to interpret radius of the tapered models compared to the truncated models. The radius of the disk where we see emission is better constrained by the truncated models, making us prefer them to the tapered models. An important factor in the difference in a_{max} between the models is because we use the dust model from Pollack et al. (1994) for the ALMA only and from Woitke et al. (2016) for the ALMA+VLA models. The ALMA+VLA models also need bigger dust grains to have sufficient emission at 8 mm. The bigger dust grains will radiate more efficiently at millimeter wavelength. For the ALMA only model, we have $a_{max} = 30\mu$m for the truncated model and $a_{max} = 207\mu$m. The more efficient emission of the tapered model due to the higher a_{max} might be one of the reasons why the disk masses are different in tapered and truncated models. The dust in ALMA+VLA models have similar $a_{max} \approx 520$ μm with power-law grain size distributions of 3.94 for the truncated model and 3.76 for the tapered model.

The envelope mass and radius of the ALMA+VLA models are significantly lower than their ALMA only counterparts. This has mostly to do with the number of points available for the fitting in the visibilities. The shorter uv-distances of the visibilities, specifically distances $< 10^2$ kλ represent the envelope while the longer uv-distances represent the disk (see Figures 4.1, 4.2, 4.3, 4.4; left plots). The visibilities from the VLA have fewer points for fitting the envelope compared to the visibilities from the ALMA, reducing their weight in the fit. The envelope is expected to be composed of smaller dust and as such should have very few centimeter-sized dust grains. This means we get very low emission at the larger VLA wavelength from the envelope. The low envelope radii of the ALMA+VLA model also accounts for the lower envelope mass compared to the ALMA only model. However, we are really concerned in fitting the disk portion of the protostar, so that we can constrain the parameters of the disk and we are able to do that fairly well; even though we do not fit the envelope ideally.

4.4.2 Model Derived Toomre's Q

The RADMC-3D synthetic models of HOPS 383 continuum in Section 4.2 has a radial profile of surface density and disk temperature embedded in them. We show these values Extracting these, we can use equation 3.3 to plot Toomre's Q as a function of radius. Figure 4.5 plots the Toomre's Q values as a function of the radius using the data from ALMA only models whereas Figure 4.6 does the same using the data from ALMA+VLA models. We assume the disk around HOPS 383 to be Keplerian since there is no evidence pointing otherwise. However, we do not know the exact mass of the central protostar, which changes the value of Ω. Therefore we plot the Q with different protostar masses ranging from 0.1 $M_\odot$ to 0.5 $M_\odot$.

We assume a dust-to-gas ratio of 1:100 for our calculation. We take an average temperature of a few slices above the mid-plane for a more consistent temperature profile of the models. The dashed lines in the figures represent the current Q values as a function of the disk radius. The disk around HOPS 383 appears to be stable with $Q > 1$ at most of the radii for the assumed protostar mass of 0.5 $M_\odot$ for the ALMA only models. For the lower protostar masses of 0.1 - 0.3 $M_\odot$, the disk may be susceptible to GI at R_c of the disk in the truncated ALMA and both the ALMA+VLA models. Following the outburst, the temperatures (and consequently c_s) are larger. We need to determine Q before the outburst to determine if GI was responsible for the outburst.

To do this, we scale the disk temperature by $\sqrt[4]{L_{*,old}/L_{*,new}}$. We use the model derived luminosities for $L_{*,new}$ and take $L_{*,\mathrm{old}} = 0.5\ L_\odot$ as we believe that the pre-outburst luminosity of HOPS 383 is underestimated due to the lack of 70 - 100 μm data. The solid lines represent the Q values prior to the outburst. Except for the ALMA tapered model, we see that prior to the outburst, the disk was gravitationally unstable around the critical radius on all other cases. Even though the protostar mass of 0.3 and 0.5 $M_\odot$ for the ALMA only models have $Q > 1$, the values are very close to 1, suggesting the disk may have been subject to GI. Furthermore, our millimeter observations are likely not sensitive to all the mass in the disk, which suggests that the disk is likely more massive than our ALMA only results. The higher the disk mass, the more likely it is to be gravitationally unstable. Hence, GI appears to be a very likely mechanism for the accretion outburst in HOPS 383.

4.5 Conclusion

We have presented detailed radiative transfer modeling to create synthetic models using MCMC fitting of the broadband SED and the visibilities obtained from the ALMA and the VLA of HOPS 383 in Orion. Using the modeling procedure from Sheehan & Eisner (2014) and Sheehan & Eisner (2017), we either fit the ALMA only visibilities or both the ALMA and the VLA visibilities with the SED of the protostar. We fit each ALMA only and the ALMA+VLA models using truncated and tapered disk types. Although both disk types were able to produce reasonable fits to the data, we prefer the truncated disk models as they constrain the radius of the disk better compared to the tapered model.

We found that the ALMA visibilities can be well modeled with a very extended envelope of over 7000 au radius. The best fit truncated model has a disk mass of 0.1 $M_\odot$ and a radius of ∼67 au, whereas the tapered model has a disk mass of 0.065 $M_\odot$ and a radius of ∼40 au. Both the ALMA only models have a very similar luminosity of ∼11 $L_\odot$. The best-fitting ALMA+VLA models are much more compact with larger disk masses of over 0.2 $M_\odot$ compared to the ALMA only models. The protostar is fit to be under-luminous in the ALMA+VLA models with $L_* = 4.6$ $L_\odot$ for the truncated model and $L_* = 4.1$ $L_\odot$ for the tapered model versus their ALMA only counterparts.

Using the radial temperature and surface density of the models, we plot Toomre's Q as a function of the disk radius, finding that in most cases, the disk is currently gravitationally stable at most radii but was most likely unstable prior to the outburst around the critical radius, providing strong indication that gravitational instability was at least partly responsible for the outburst.

In our models, we were mostly concerned with constraining the disk parameters to understand the mechanism of the outburst, which we are able to do fairly well. Our envelope parameters, however, are not as well constrained. This is due to the fewer number of points available in the shorter uv-distances of the visibilities, especially the VLA visibilities, where we have very little emission from the envelope at 8 mm. In order to extend the constrains to the envelope, it would be beneficial to model visibilities from shorter uv-distances.

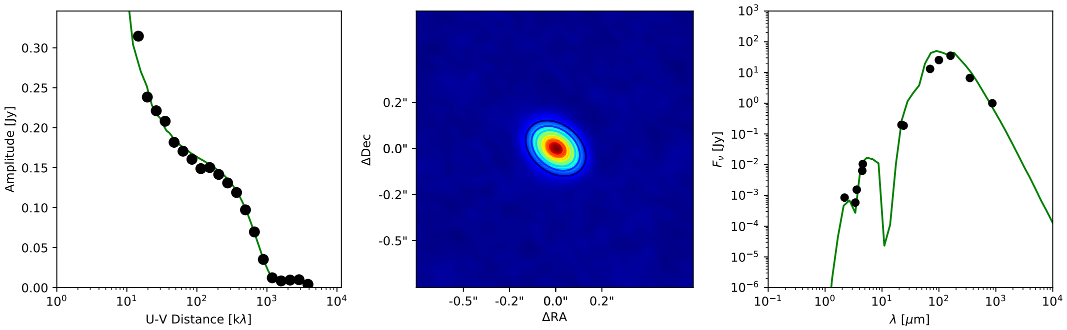

Fig. 4.1.—: Best fit model to HOPS 383 at 870 μm using the truncated disk. The left panel shows the circularly averaged visibility amplitudes of the data (black dots) compared to the model (green line). The middle panel shows the synthetic model with the contours of the best fitting model overlaid. The right panel shows the model of the SED (green line) overlaid on the SED data from the literature.

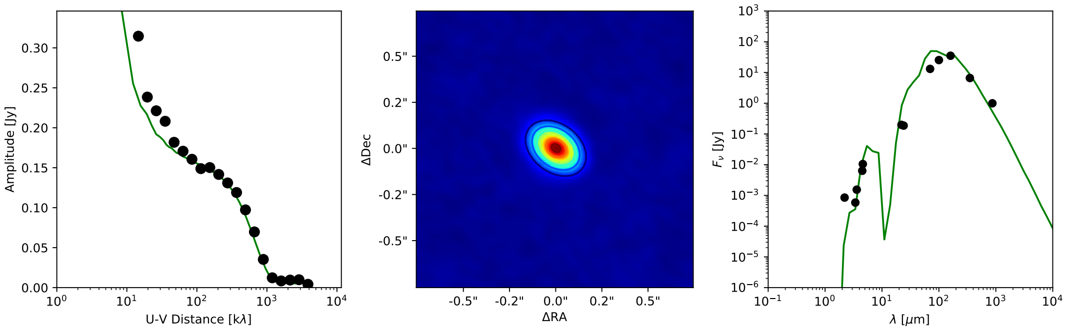

Fig. 4.2.—: Best fit model to HOPS 383 at 870 μm using the tapered disk. The left panel shows the circularly averaged visibility amplitudes of the data (black dots) compared to the model (green line). The middle panel shows the synthetic model with the contours of the best fitting model overlaid. The right panel shows the model of the SED (green line) overlaid on the SED data from the literature.

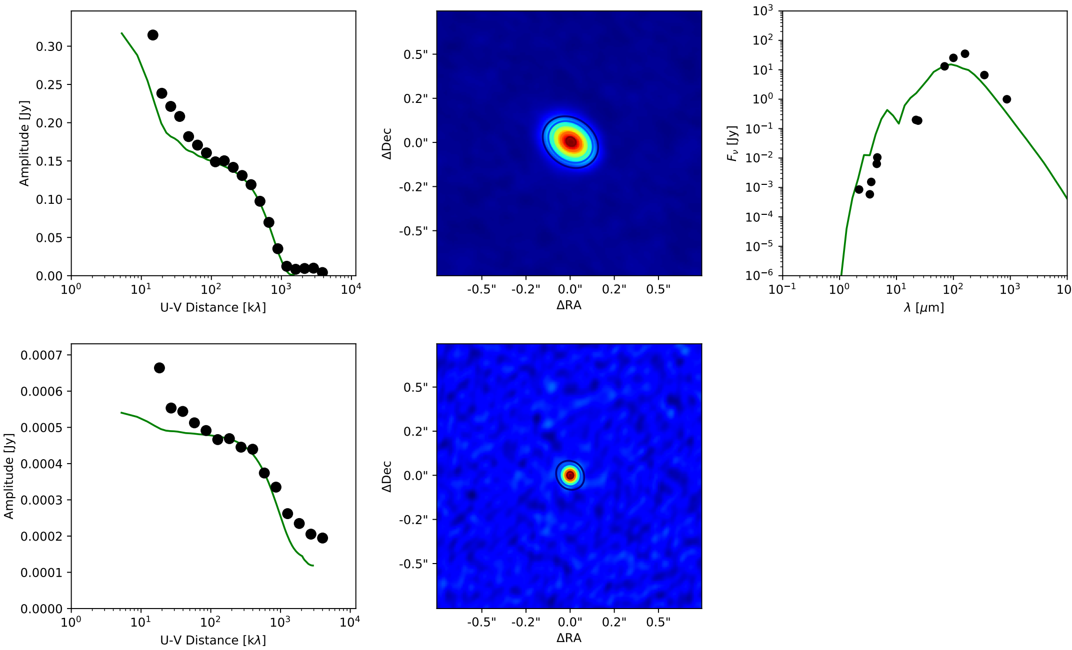

Fig. 4.3.—: Best fit model to HOPS 383 at 870 μm (top) and 8 mm (bottom) using the truncated disk. The 870 μm data comes from the ALMA and 8 mm comes from the VLA. The left panels show the circularly averaged visibility amplitudes of the data (black dots) compared to the model (green line). The middle panels show the synthetic model to the ALMA (top) and the VLA (bottom) with the contours of the best fitting model overlaid. The right panel shows the model of the SED (green line) overlaid on the SED data from the literature.

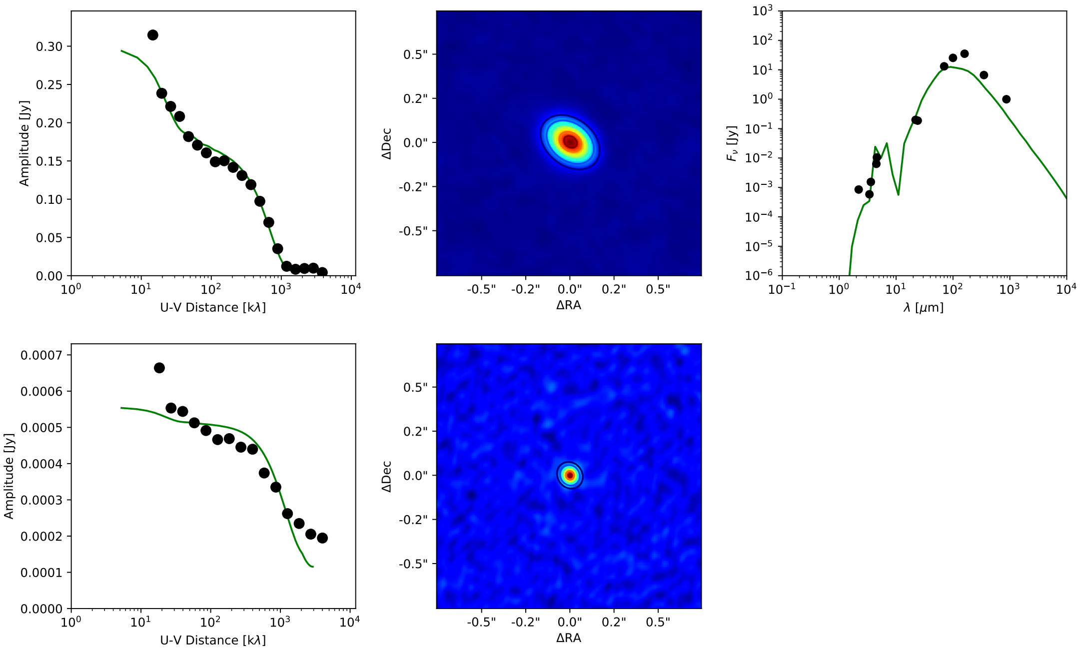

Fig. 4.4.—: Best fit model to HOPS 383 at 870 μm (top) and 8 mm (bottom) using the tapered disk. The 870 μm data comes from the ALMA and 8 mm comes from the VLA. The left panels show the circularly averaged visibility amplitudes of the data (black dots) compared to the model (green line). The middle panels show the synthetic model to the ALMA (top) and the VLA (bottom) with the contours of the best fitting model overlaid. The right panel shows the model of the SED (green line) overlaid on the SED data from the literature.

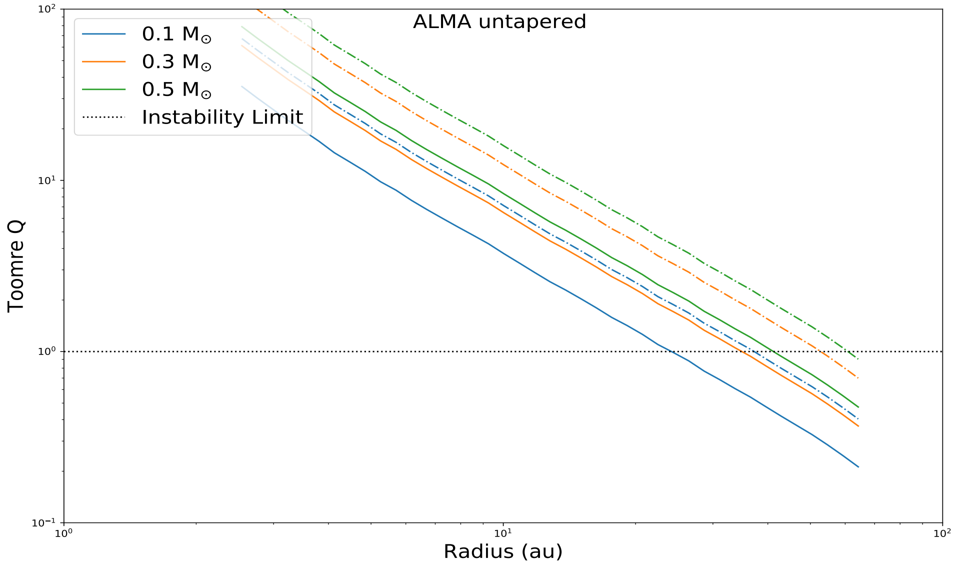

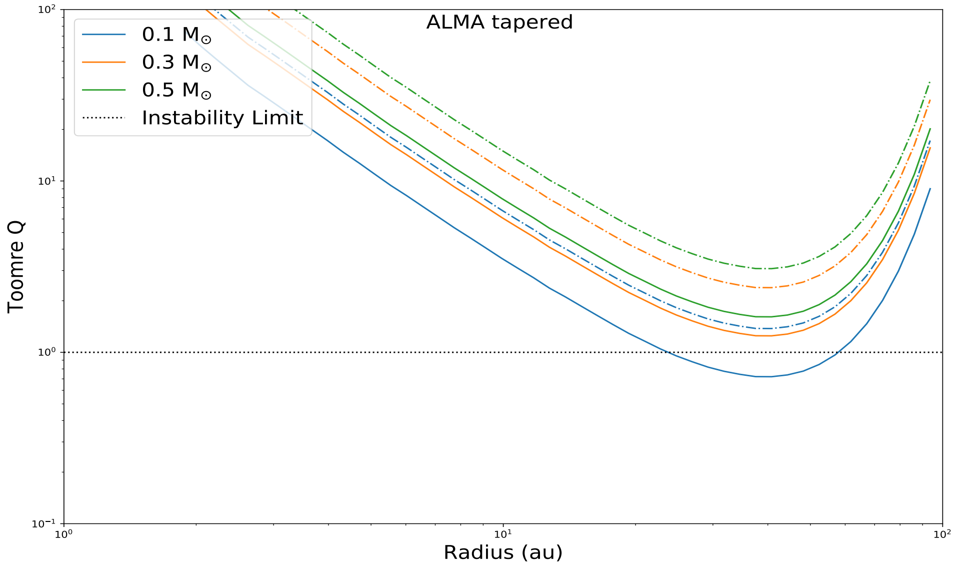

Fig. 4.5.—: Toomre's Q as a function of radius for the disk of HOPS 383 using the ALMA only models for different protostar masses. The dashed lines represent the current Q values and the solid lines repersent the Q values prior to the outburst obtained by scaling the temperature by a factor of $\sqrt[4]{0.5L_\odot/L_*}$, where 0.5 $L_\odot$ is the luminosity of HOPS 383 before the outburst. The dotted horizontal line marks the value of $Q = 1$. Currently, the disk seems to be gravitationally stable for most cases. The truncated model seems to have been unstable around its critical radius. Although the tapered model has $Q > 1$, for all cases before the outburst too, the values are very close to 1, suggesting that the disk may have been gravitationally unstable before, causing the accretion burst.

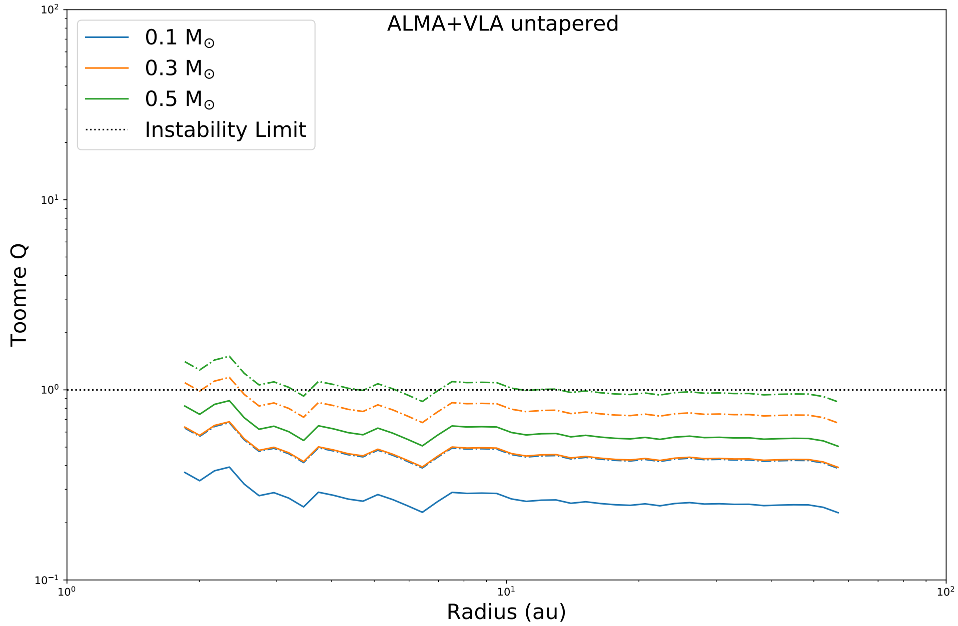

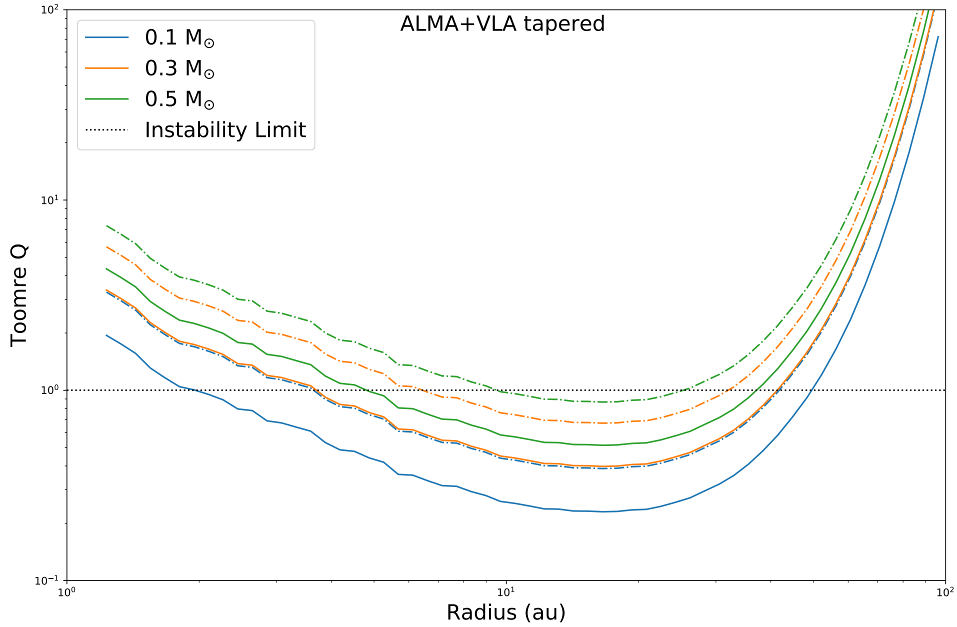

Fig. 4.6.—: Toomre's Q as a function of radius for the disk of HOPS 383 using the ALMA+VLA models for different protostar masses. The different lines reperesent the same as Figure 4.5. The large disk mass compared to ALMA only models suggest the disk is currently marginally unstable at the critical radius, R_c in most cases. Prior to the outburst, we see that the disk is gravitationally unstable for all the cases, suggesting GI was at least partly responsible for the accretion burst.

Table 4.1:: List of parameters used in the modeling

Parameter	Description	Free/Fixed	Values/Range
Stellar Parameters			
M_* ($M_\odot$)	Stellar mass	Fixed	1.0
T_* (K)	Stellar temperaure	Fixed	4000
L_* ($L_\odot$)	Stellar luminosity	Free	[-1, 2.5] (log space)
Disk Parameters			
Disk Type	Only used if tapered disk type is chosen	Fixed	Tapered
M_{disk} ($M_\odot$)	Disk mass	Free	[-10, -1.5] (log space)
$R_{in,disk}$ (au)	Inner radius of the disk	Free	[-1.0, 4.0] (log space)
R_{disk} (au)	Disk radius	Free	[0.0, 4.0] (log space)
h_0 (au)	Disk scale height at 1 au	Free	[0.01, 0.5]
γ	Surface density power-law exponent	Free	[-0.5, 2.0]
β ($L_\odot$)	Disk scale height exponent	Free	[0.5, 1.5]
Envelope Parameters			
M_{env} ($M_\odot$)	Envelope mass	Free	[-10, -1] (log space)
$R_{in,env}$ (au)	Inner radius for the envelope	Fixed	$R_{in,disk}$
R_{env} (au)	Envelope radius	Free	[3.0, 4.5] (log space)
R_c (au)	Critical radius of the envelope	Fixed	R_{disk}
f_{cav}	Ratio of cavity density to normal density	Free	[0.0, 1.0]
ξ	Cavity opening angle	Free	[0.5, 1.5]
Dust Parameters			
Dust File	Only used in ALMA+VLA models to include dust opacities for VLA visibilities	Fixed	Woitke et al. (2016)
a_{max} (μm)	Maximum dust grain size	Free	[0.0, 5.0] (log space)
p	Dust grain size power-law	Free	[2.5, 4.5]
Viewing Parameters			

i (°)	Inclination	Free	[0.0, 90.0]
$P.A.$ (°)	Position Angle	Free	[0.0, 180.0]
x_0 ($''$)	Horizontal Offset	Fixed	0.0
y_0 ($''$)	Vertical Offset	Fixed	0.0
d_{pc} (pc)	Distance to the system	Fixed	400
A_k	K-band extinction	Fixed	0

Table 4.2:: HOPS 383 photometry data used for the SED

Wavelength (μm)	Flux Density (mJy)	RMS (mJy bm^{-1})	Instrument [a]	Date
2.2	0.850	0.0272	NEWFIRM	2009 Nov 25
3.4	0.585	0.0969	WISE	2010 Mar 8 Sep 16
3.6	1.54	0.0770	IRAC	2009 Oct 23
4.5	6.34	0.317	IRAC	2009 Oct 23
4.6	10.5	0.358	WISE	2010 Mar 8 Sep 16
22	198	16.8	WISE	2006 Oct 20
24	187	9.87	MIPS	2008 Apr 19
70	13100	150	PACS	2010 Sep 10
100	25400	1360	PACS	2010 Oct 8
160	35100	2010	PACS	2010 Sep 1028
350	6620	2650	SABOCA	2011 Sep 16
870	996	199	LABOCA	2010 Oct 24

---

[a] NEWFIRM – NOAO (National Optical Astronomy Observatory) Extremely Wide-Field Infrared Imager, WISE – Wide-Field Infrared Survey Explorer, IRAC – Infrared Array Camera, MIPS – Multiband Imaging Photometer, PACS – Photodetector Array Camera and Spectrometer, SABOCA – Submillimetre APEX (Atacama Pathfinder Experiment) Bolometer Camera, LABOCA – Large APEX Bolometer Camera

Table 4.3:: Best fit model parameters for HOPS 383.

Parameter (unit)	ALMA		ALMA+VLA	
	Truncated	Tapered	Truncated	Tapered
β	$0.77^{+0.04}_{-0.04}$	$0.57^{+0.02}_{-0.02}$	$0.77^{+0.03}_{-0.04}$	$0.79^{+0.04}_{-0.06}$
f_{cav}	$0.11^{+0.02}_{-0.02}$	$0.05^{+0.01}_{-0.01}$	$0.63^{+0.06}_{-0.06}$	$0.28^{+0.07}_{-0.10}$
γ	$0.23^{+0.04}_{-0.06}$	$-0.19^{+0.05}_{-0.07}$	$1.68^{+0.19}_{-0.10}$	$0.59^{+0.06}_{-0.04}$
h_0(au)	$0.13^{+0.01}_{-0.01}$	$0.09^{+0.01}_{-0.01}$	$0.13^{+0.01}_{-0.00}$	$0.08^{+0.02}_{-0.03}$
$i(^\circ)$	$51.3^{+0.3}_{-0.3}$	$51.3^{+0.5}_{-0.5}$	$49.6^{+1.3}_{-1.2}$	$51.2^{+0.5}_{-0.8}$
ξ	$1.15^{+0.01}_{-0.01}$	$1.17^{+0.02}_{-0.02}$	$0.99^{+0.03}_{-0.02}$	$1.07^{+0.05}_{-0.07}$
$L_*(L_\odot)$	$10.8^{+0.8}_{-0.8}$	$11.1^{+0.9}_{-0.7}$	$4.6^{+0.5}_{-0.3}$	$4.1^{+0.2}_{-0.2}$
$M_{disk}(M_\odot)$	$0.104^{+0.011}_{-0.009}$	$0.065^{+0.008}_{-0.006}$	$0.257^{+0.024}_{-0.014}$	$0.209^{+0.014}_{-0.014}$
$M_{env}(M_\odot)$	$2.477^{+0.239}_{-0.270}$	$2.478^{+0.507}_{-0.635}$	$0.148^{+0.059}_{-0.052}$	$0.080^{+0.022}_{-0.012}$
R_{disk}(au)	$67.43^{+0.48}_{-1.05}$	$39.84^{+0.87}_{-0.87}$	$57.44^{+1.55}_{-1.11}$	$19.19^{+0.67}_{-0.90}$
R_{env}(au)	$7353.86^{+451.70}_{-534.43}$	$7273.63^{+993.71}_{-1127.50}$	$3377.78^{+786.92}_{-862.09}$	$2407.87^{+381.15}_{-250.59}$
R_{in}(au)	$2.60^{+0.43}_{-0.72}$	$1.77^{+0.29}_{-0.28}$	$1.60^{+0.48}_{-0.26}$	$1.13^{+0.16}_{-0.13}$
$a_{max}(\mu$m)	$30.42^{+7.84}_{-5.89}$	$207.08^{+14.06}_{-13.29}$	$524.37^{+113.44}_{-105.60}$	$516.94^{+63.99}_{-68.41}$
p	$3.49^{+0.12}_{-0.07}$	$3.60^{+0.08}_{-0.07}$	$3.94^{+0.05}_{-0.04}$	$3.76^{+0.12}_{-0.16}$
$P.A(^\circ)$	$49.01^{+0.52}_{-0.48}$	$49.79^{+0.46}_{-0.74}$	$49.56^{+1.15}_{-1.40}$	$48.85^{+0.87}_{-1.09}$

Chapter 5

Conclusions and Future Work

In this thesis, I have presented observational results of the structure of the disk envelope and chemical signatures around the youngest known outbursting protostar, HOPS 383. Using the results from the observations, I test the models that describe the effect of accretion bursts on the chemistry of a highly embedded protostellar system. In addition, I have also characterized the general properties such as the mass, radius, and temperature of the disk around HOPS 383 using the resolved continuum emission from the ALMA and the VLA and used these properties to test gravitational instability as the cause of the outburst. I have outlined the results of the specific Chapters of this thesis and their implications here.

5.1 Chapter Summaries

In Chapter 2, I presented molecular line emissions of HOPS 383 after the outburst obtained from the SMA. This gives new ways to identify signatures of outburst in protostars in the last 100 years. The evaporating CO due to the rise in temperature reacts and destroys the N_2H^+ in the surrounding envelope, forming HCO^+ (Visser & Bergin 2012). Consequently, I show that in HOPS 383, N_2H^+ is reduced at the protostar position, where HCO^+ peaks. There is a spatial overlap between the emitting regions of CO and N_2H^+ as the destruction of N_2H^+ takes roughly 50 - 100 years. Observations of N_2H^+ and HCO^+ emission maps around protostars can serve as a way to indirectly identify young systems that have recently undergone outburst. I also observed the $C^{18}O$ emission to test another signature of outburst but the $C^{18}O$ emitting region could not be identified due to contamination by emission from a nearby molecular cloud at a similar velocity range. Follow-up observation of $C^{18}O$ around HOPS 383 with a more compact spectral window could help remove the contamination and determine the $C^{18}O$ emitting region.

In Chapter 3, I presented the ALMA and the VLA continuum images of HOPS 383. The continuum resolves a dense structure orthogonal to the outflow, suggestive of a protostellar disk. I found an average disk temperature of 50 K based on the bolometric luminosity of 7.8 $L_\odot$ for HOPS 383 following the outburst. Using a 50 K disk temperature and integrated flux density from the continuum data, I calculated disk masses of $\sim$0.043 $M_\odot$ and $\sim$0.15 $M_\odot$ from the ALMA and the VLA, respectively. Testing for gravitational stability, I found that the ALMA disk mass gives Toomre's $Q = 2.82$, suggesting that the disk is currently stable. I only use the ALMA disk mass because the appropriate dust opacity for the VLA observations at 9 mm is uncertain. Prior to the outburst, the disk temperature would likely be around 30 K, so scaling the temperature, Q would be scaled by $(50/30)^{0.5}$, lowering Q. In addition, the ALMA continuum might underestimate the disk mass as the observation is most likely not sensitive to all the mass in the disk, which makes gravitational instability a very possible mechanism of outburst. Future observations of HOPS 383 system in multiple wavelengths should help to better constrain the disk mass of the system.

In Chapter 4, I presented radiative transfer modeling using MCMC fitting of the ALMA and the VLA visibilities along with the broadband SED of HOPS 383 to constrain the parameters of HOPS 383. Fitting both visibilities and the SED simultaneously resolves the degeneracies that can arise when fitting either data set separately. Each ALMA only and the ALMA+VLA models were fit using truncated and tapered disk types, in order to observe any large differences in the parameters between the two types and determine which one better fits the data sets. I found that both disk types were able to fit the data reasonably well, but, I preferred the truncated disk for both models as it was difficult to constrain the disk radius properly in the tapered models. The ALMA only models have a smaller disk and higher luminosity compared to the ALMA+VLA model. The envelopes of the ALMA only models are much larger than their ALMA+VLA counterparts. This is probably due to lack of emission from the envelope in the VLA observation at the longer wavelength of 8 mm, and the higher luminosities of ALMA only models would make the disk too bright for the ALMA+VLA models.

Using the temperature and surface density embedded in the models, I was able to plot Toomre's Q as a function of disk radius for all the models. I found $Q > 1$ for most cases following the outburst, suggesting the disk is currently gravitationally stable. However, scaling the temperature and c_s to before the outburst revealed that in majority of the scenarios, the disk was subject to GI near the critical radius. Thus, GI appears to be a major factor of the accretion burst in HOPS 383. Due to the fewer number of points in the short uv-distances, I was unable to fit the envelope parameters as well as the disk parameters. However, this thesis is mostly concerned with the disk parameters, which were more or less consistent through the models.

5.2 Future Work

This thesis presents strong evidence in favor of episodic accretion being the primary method of accretion in the early stages of YSOs. Future surveys can look for the chemical signatures of N_2H^+, HCO^+, and C18O to determine if a protostar has recently undergone an outburst. However, another key unknown in star formation process is the origin of multiplicity. Over 50% of low mass stars are found in multiple systems with an average separation of 50 au (Raghavan et al. 2010; Lada 2006). Hence, it is important to understand the origin of multiplicity to have a complete understanding of star formation process.

The formation of multiple star system is generally agreed to begin in the early phases of star formation when the surrounding disk is still massive (e.g. Tohline 2002). While collapsing, the massive disk can fragment several times due to GI, leading to formation of multiple systems (Kratter et al. 2010; Vorobyov 2010; Tobin et al. 2016). As this thesis shows, GI might be one of the primary causes of accretion bursts in YSOs, and it may be possible to discover formation of multiple systems in recently outbursting protostars or find signatures of bursts in already known multiple systems.

Therefore, it is important to have a comprehensive study of all the known nearby multiple systems using different instruments. Most young multiple systems are deeply embedded and have very small separations. The only way to observe them is by using very high-resolution radio continuum observations. Likewise, in some cases, a multiple systems can be optically thin at the observing wavelength in radio but be visible to optical imaging.

To establish a comprehensive list of all the multiple systems in Orion, I have started to compare images from the Hubble Space Telescope (HST) of the HOPS sources with the ALMA observations. I have found that most of the multiple systems in ALMA that were not recognized by the HST is because the multiples are very close to one another (sub-arcsecond difference between the sources). One such example of a binary found in ALMA which was not found in HST is shown in Figure 5.1. Once the multiple systems in Orion are identified, there is a potential to create a pipeline to quickly identify newly observed systems for multiplicity and constrain the possibility of an outburst. The high number of HOPS sources can also yield statistically meaningful results. Finally, with the advent of higher resolution ALMA and the upcoming Next Generation Very Large Array (ngVLA), it will be possible to resolve systems that are < 50 au scales, helping to answer the questions about multiplicity.

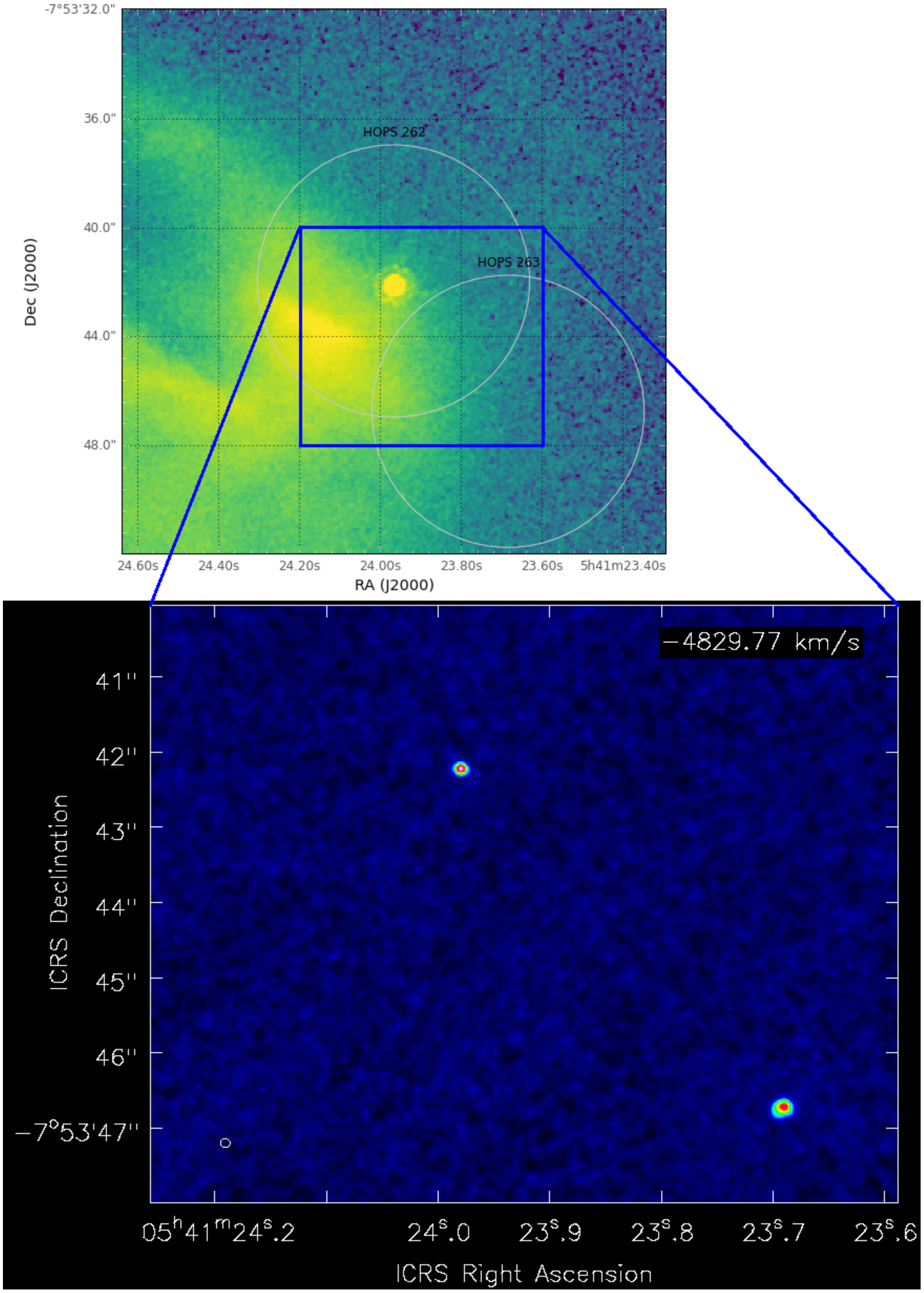

Fig. 5.1.—: HOPS 262 and HOPS 263 observed with the HST and the ALMA. The ALMA observation clearly resolves both the protostars but HOPS 263 is not seen in the HST image.

References

Ábrahám, P., Kóspál, A., Csizmadia, S., et al. 2004, A&A, 419, L39

Arce, H. G., Mardones, D., Corder, S. A., et al. 2013, ApJ, 774, 39

Adams, F. C., Lada, C. J., & Shu, F. H. 1987, ApJ, 312, 788

André, P., Ward-Thompson, D., & Barsony, M. 1993, ApJ, 406, 122

Andrews, S. M., Wilner, D. J., Hughes, A. M., Qi, C., & Dullemond, C. P. 2010, ApJ, 723, 1241

Anglada, G., Villuendas, E., Estalella, R., et al. 1998, AJ, 116, 2953

Armitage P. J., Livio M., & Pringle J. E., 2001, MNRAS, 324, 705

Aso, Y., Ohashi, N., Saigo, K., et al. 2015, ApJ, 812, 27

Audard, M., Abrahám, P., Dunham, M. M., et al. 2014, in Protostars and Planets VI, ed. H. Beuther, R. Klessen, K. Dullemond, & T. Henning (Tucson, AZ: Univ. Arizona Press), 387

Baraffe, I., Chabrier, G., & Gallardo, J. 2009, ApJ, 702, L27

Baraffe, I., Vorobyov, E. I., & Chabrier, G. 2012, ApJ, 756, 118

Basu, S. 1997, ApJ, 485, 240

Beckwith, S. V. W., Sargent, A. I., Chini, R. S., & Guesten, R. 1990, AJ, 99, 924

Bergin, E. A., & Tafalla, M. 2007, ARA&A, 45, 339

Bohlin, R. C., Savage, B. D., & Drake, J. F. 1978, ApJ, 224, 132

Bonnell, I., & Bastien, P. 1992, ApJ, 401, L31

Charnley, S. B., Rodgers, S. D., & Ehrenfreund, P. 2001, A&A, 378, 1024

Chen, H., Myers, P. C., Ladd, E. F., & Wood, D. O. S. 1995, ApJ, 445, 377

Chiang, E. I., & Goldreich, P. 1999, ApJ, 519, 279

Chiang, H., Looney, L. W., Tassis, K., Mundy, L. G., & Mouschovias, T. C. 2008, ApJ, 680, 474

Codella, C., Cabrit, S., Gueth, F., et al. 2014, A&A, 568, L5

Dopita A., 1978, A&A, 63, 237

Dullemond, C. P. 2012, RADMC-3D: A Multi-purpose Radiative Transfer Tool, Astrophysics Source Code Library, http://ascl.net/1202.015

Dunham M. M., Evans Neal J. I., Terebey S., Dullemond C. P., Young C. H., 2010, ApJ, 710, 470

Dunham, M. M., Stutz, A. M., Allen, L. E., et al. 2014, in Protostars and Planets VI, ed. H. Beuther, R. Klessen, K. Dullemond, & T. Henning (Tucson, AZ: Univ. Arizona Press), 195

Eisner, J. A. 2012, ApJ, 755, 23

Eisner, J. A., Hillenbrand, L. A., Carpenter, J. M., & Wolf, S. 2005, ApJ, 635, 396

Evans, N.J., II 1999, ARA&A, 37, 311

Evans, N. J., II, et al. 2003, PASP, 115, 965

Evans, N. J., II, Dunham, M. M., Jrgensen, J. K., et al. 2009, ApJS, 181, 321

Fatuzzo, M., Adams, F. C., & Myers, P. C. 2004, ApJ, 615, 813

Fischer, W. J., Megeath, S. T., Furlan, E., et al. 2017, ApJ, 840, 69

Fischer, W. J., Megeath, S. T., Tobin, J. J., et al. 2012, ApJ, 756, 99

Foreman-Mackey, D., Hogg, D. W., Lang, D., Goodman, J. 2013, PASP, 125, 306

Foster, P. N., & Chevalier, R. A. 1993, ApJ, 416, 303

Frimann, S, Jorgensen, J. K., Dunham, Michael M., et al. 2017, A&A, 602, 120

Furlan, E., Fischer, W. J., Ali, B., et al. 2016, ApJS, 224, 5

Galli, D., & Shu, F. H. 1993, ApJ, 417, 220

Galvàn-Madrid, R., Rodrguez, L. F., Liu, H. B., et al. 2015, ApJ, 806, L32

Gammie, C. F. 1999, in ASP Conf. Ser. 160, Astrophysical Discs: An EC Summer School, ed. J. A. Sellwood & J. Goodman (San Francisco, CA: ASP), 122

Goldsmith, P. F. 1987, in Astrophysics and Space Science Library, Vol. 134, Interstellar Processes, ed. D. J. Hollenbach & H. A. Thronson Jr., 5170

Graham, J. A., & Frogel, J. A. 1985, ApJ, 289, 331

Greene T. P., Aspin C., Reipurth B., 2008, AJ, 135, 1421

Hartmann, L., & Kenyon, S. J. 1996, ARA&A, 34, 207

Henriksen, R., André, P., & Bontemps, S. 1997, A&A, 323, 549

Herbig G. H., 1977, ApJ, 217, 693

Hunter, C. 1977, ApJ, 218, 834

Jørgensen, J. K., van Dishoeck, E. F., Visser, R., et al. 2009, A&A, 507, 861

Jørgensen, J. K., Visser, R., Williams, J. P., & Bergin, E. A. 2015, A&A, 579, A23

Kenyon, S. J., Calvet, N., & Hartmann, L. 1993, ApJ, 414, 676

Kenyon, S. J., & Hartmann, L. W. 1995, ApJS, 101, 117

Kenyon, S. J., Hartmann, L. W., Strom, K. M., & Strom, S. E. 1990, AJ, 99, 869

Kratter, K., & Lodato, G. 2016, ARA&A, 54, 271

Kratter, K. M., Matzner, C. D., Krumholz, M. R., & Klein, R. I. 2010, ApJ, 708, 1585

Kryukova, E., Megeath, S. T., Gutermuth, R. A., et al. 2012, AJ, 144, 31

Lada, C. 2006, ApJ, 640, 63

Lada, C. J. 1987, in IAU Symposium, Vol. 115, Star Forming Regions, ed. M. Peimbert & J. Jugaku, 117

Lada, C. J. 1991, NATO ASIC Proc. 342, The Physics of Star Formation and Early Stellar Evolution (Dordrecht: Kluwer), 329

Lada, C. J., & Lada, E. A. 2003, ARA&A, 41, 57

Lada, C. J., & Wilking, B. A. 1984, ApJ, 287, 610

Larson, R. B. 1969, MNRAS, 145, 271

Lee, C.-F., Hirano, N., Zhang, Q., et al. 2014, ApJ, 786, 114

Lee, C.-F., Ho, P. T. P., Hirano, N., et al. 2007, ApJ, 659, 499

Lindberg, J. E., Jørgensen, J. K., Brinch, C., et al. 2014, A&A, 566, A74

Li, Z.-Y., & Shu, F. H. 1997, ApJ, 475, 237

Lynden-Bell, D., & Pringle, J. E. 1974, MNRAS, 168, 603

Mac Low, M. & Klessen, R. S. 2004, Reviews of Modern Physics, 76, 125

Mathis, J. S., Rumpl, W., & Nordsieck, K. H. 1977, ApJ, 217, 425

McKee, C. F. & Ostriker, E. C. 2007, ARA&A, 45, 565

McMullin, J. P., Waters, B., Schiebel, D., Young, W., & Golap, K. 2007, in Astronomical Society of the Pacific Conference Series, Vol. 376, Astronomical Data Analysis Software and Systems XVI, ed. R. A. Shaw, F. Hill, & D. J. Bell, 127

Megeath, S. T., Gutermuth, R., Muzerolle, J., et al. 2012, AJ, 144, 192

Murillo, N. M., Lai, S.-P., Bruderer, S., Harsono, D., & van Dishoeck, E. F. 2013, A&A, 560, A103

Muzerolle, J., Furlan, E., Flaherty, K., Balog, Z., & Gutermuth, R. 2013, Nature, 493, 378

Myers, P. C., & Ladd, E. F. 1993, ApJ, 413, L47

Offner, S. S. R., & McKee, C. F. 2011, ApJ, 736, 53

Ossenkopf, V., & Henning, T. 1994, A&A, 291, 943

Owen, J. E., & Jacquet, E. 2015, MNRAS, 446, 3285

Penston, M. V. 1969, MNRAS, 145, 457

Plunkett, A. L., Arce, H. G., Mardones, D. et al. 2015, Nature, 527, 70

Pollack, J. B., Hollenbach, D., Beckwith, S., et al. 1994, ApJ, 421, 615

Persson, M. V.. 2014 (figshare), https://doi.org/10.6084/m9.figshare.1121574.v2

Pudritz R. E., Ouyed R., Fendt C., Brandenburg A., 2007, in Protostars and Planets V, ed. Reipurth B., Jewitt D., Keil K., (Tucson, AZ: Univ. Arizona Press), 277

Raghavan, D., McAlister, H. A., Henry, T. J., et al. 2010, ApJS190, 1

Reipurth B., 1989, Nature, 340, 42

Reipurth, B., & Aspin, C. 2004, ApJ, 606, L119

Robitaille, T. P., Whitney, B. A., Indebetouw, R., & Wood, K. 2007, ApJS, 169, 328

Rodríguez, L. F. 1997, in IAU Symp. 182, Herbig-Haro Flows and the Birth of Stars, ed. B. Reipurth & C. Bertout (Cambridge: Cambridge Univ. Press), 83

Safron, E. J., Fischer, W. J., Megeath, S. T., et al. 2015, ApJ, 800, L5

Sault, R. J., Teuben, P. J., & Wright, M. C. H. 1995, in ASP Conf. Ser. 77, Astronomical Data Analysis Software and Systems IV, ed. R. A. Shaw, H. E. Payne, & J. J. E. Hayes (San Francisco, CA: ASP), 433

Shang H., Li Z.-Y., Hirano N., 2007, in Protostars and Planets V, ed. Reipurth B., Jewitt D., Keil K., (Tucson, AZ: Univ. of Arizona Press), 261

Sheehan, P. D., & Eisner, J. A. 2014, ApJ, 791, 19

Sheehan, P. D., & Eisner, J. A. 2017, ApJ, 851, 45

Shu, F. H. 1977, ApJ, 214, 488

Shu, F. H., Adams, F. C., & Lizano, S. 1987, ARA&A, 25, 23

Shu, F., Najita, J., Ostriker, E., et al. 1994, ApJ, 429, 781

Stutz, A. M., Tobin, J. J., Stanke, T., et al. 2013, ApJ, 767, 36

Terebey, S., Shu, F. H., & Cassen, P. 1984, ApJ, 286, 529

Testi, L., Birnstiel, T., Ricci, L., et al. 2014, in Protostars and Planets VI, ed. H. Beuther . Klessen, K. Dullemond, & T. Henning (Tucson, AZ: Univ. of Arizona Press), 339

Tobin, J. J., Bergin, E. A., Hartmann, L., et al. 2013, ApJ, 765, 18

Tobin, J. J., Bos, S. P., Dunham, M. M., Bourke, T. L., & van der Marel, N. 2018, ApJ, 856, 164

Tobin, J. J., Chandler, C. J., Wilner, D. J., et al. 2013, ApJ, 779, 93

Tobin, J. J., Hartmann, L., Chiang, H.-F., et al. 2012, Nature, 492, 83

Tobin, J. J., Kratter, K. M., Persson, M. V., et al. 2016, Nature, 538, 483

Tobin, J. J., Looney, L. W., Mundy, L. G., Kwon, W., & Hamidouche, M. 2007, ApJ, 659, 1404

Tohline, J. 2002, ARA&A, 40, 349

Tychoniec, Ł., Tobin, J. J., Karska, A., et al. 2018, ApJS, 238, 19

Ulrich, R. K. 1976, ApJ, 210, 377

Visser, R., & Bergin, E. A. 2012, ApJ, 754, L18

Visser, R., Bergin, E. A. & Jørgensen J. K. 2015, A&A, 577, A102

Visser R., Doty S. D., & van Dishoeck E. F., 2011, A&A, 534, A132

Vorobyov, E. 2010, ApJ, 723, 1294

Vorobyov, E. I., & Basu, S. 2005, MNRAS, 360, 675

Vorobyov, E. I., & Basu, S. 2006, ApJ, 650, 956

Vorobyov, E. I., Baraffe, I., Harries, T., & Chabrier, G. 2013, A&A, 557, A35

Wachmann, A. A. 1939, IAU Circ., 738, 1

Williams, J. P., & Cieza, L. A. 2011, ARA&A, 49, 67

Whitney, B. A., Wood, K., Bjorkman, J. E., & Wolff, M. J. 2003b, ApJ, 591, 1049

Woitke, P., Min, M., Pinte, C., et al. 2016, A&A, 586, A103

Yen, H.-W., Koch, P. M., Takakuwa, S., et al. 2015, ApJ, 799, 193

Yen, H.-W., Koch, P. M., Takakuwa, S., et al. 2015, ApJ, 834, 178

Zhu, Z., Hartmann, L., Calvet, N., Hernandez, J., Muzerolle, J., & Tannirkulam, A.-K. 2007, ApJ, 669, 483

Zhu, Z., Hartmann, L., Calvet, N., Hernandez, J., Tannirkulam, A.-K., & DAlessio, P. 2008, ApJ, 684, 1281

Zhu, Z., Hartmann, L., & Gammie, C. 2009b, ApJ, 694, 1045

Zuckerman, B., & Evans, N. J., II. 1974, ApJ, 192, L149